We are IntechOpen,
the world's leading publisher of
Open Access books
Built by scientists, for scientists

4,800
Open access books available

122,000
International authors and editors

135M
Downloads

154
Countries delivered to

Our authors are among the

TOP 1%
most cited scientists

12.2%
Contributors from top 500 universities

CLARIVATE ANALYTICS

BOOK CITATION INDEX

INDEXED

WEB OF SCIENCE™

Selection of our books indexed in the Book Citation Index
in Web of Science™ Core Collection (BKCI)

Interested in publishing with us?
Contact book.department@intechopen.com

Numbers displayed above are based on latest data collected.
For more information visit www.intechopen.com

All-Optical Signal Processing with Semiconductor Optical Amplifiers and Tunable Filters

Xinliang Zhang, Xi Huang, Jianji Dong, Yu Yu, Jing Xu and Dexiu Huang
Wuhan National Laboratory for Optoelectronics,
Huazhong University of Science and Technology
P.R.China

1. Introduction

All-optical signal processing has been and is receiving more and more attention all over the world because it can increase the capacity of the optical networks greatly in avoiding of the Optical-Electrical-Optical (O/E/O) conversion process, and it can also reduce the system power consumption to a great extend and then increase the system stability. All-optical signal processing can be widely used in optical signal regeneration and switching in next-generation optical networks (Yoo 1996; Danielsen et al. 1998; Saruwatari 2000), such as Optical Time Division Multiplexing (OTDM), Optical Orthogonal Frequency Division Multiplexing (OOFDM), Optical Code Division Multiplexing Accessing (OCDMA), Optical Packet Switching (OPS) and so on. There are many different elemental functions in all-optical signal processing: all-optical wavelength conversion, all-optical logic operation, all-optical 3R regeneration, all-optical format conversion, all-optical sampling, all-optical time demultiplexing, all-optical buffering, etc. It should be mentioned that all-optical wavelength conversion is one of the most important technologies, and it is the basis of other functions. In past two decades, many schemes have been proposed to demonstrate all-optical signal processing functions, and nonlinearities in passive and active waveguides, such as high nonlinear fiber (Olsson et al., 2001), periodic-poled $LiNbO_3$ (Langrock et al., 2006), silicon-based waveguides (Haché & Bourgeois 2000), chalcogenide-based waveguides (Ta'eed et al., 2006) and semiconductor optical amplifiers (SOAs) (Liu et al., 2006; Stubkjaer 2000) , are elemental mechanisms for these schemes. SOA is one of powerful candidates for all-optical signal processing because of its various nonlinear effects, low power consumption, small footprint and possibility to be integrated, therefore, SOAs have been receiving the most widely attention and have been exploited to realize nearly all functions for all-optical signal processing.

In SOAs, nonlinear effects such as cross-gain modulation (XGM), cross-phase modulation (XPM), four-wave mixing and transient cross-phase modulation can all be exploited to demonstrate all-optical signal processing functions (Durhuus et al., 1996; Stubkjaer 2000). Taking all-optical wavelength conversion as an example, XGM wavelength conversion has some advantages such as simple structure, large dynamic optical power range, high conversion efficiency and large operation wavelength range, but it also has some problems

such as extinction ratio degradation and chirp (Durhuus et al., 1996); XPM wavelength conversion has some characteristics such as good output performance but small dynamic range and difficult to control and fabricate (Durhuus et al., 1996); FWM wavelength conversion (Kelly et al., 1998) is bitrate and format transparent but low conversion efficiency and narrow operation wavelength range; transient XPM conversion is inherent high operation speed but low conversion efficiency.

While used in all-optical signal processing, the input probe signals of SOAs will experience amplitude and phase variations which are induced by carrier density or distribution variations taken by other input pump signals. The optical spectra of the input signals will experience broadening and shifting processes in which the information to be processed is included. Therefore, the SOA can be regarded as spectrum transformer. Combing with appropriate filtering process, all-optical signal processing function can be realized correspondingly. For different filtering processes, we can demonstrate different signal processing functions.

Regarding filtering processes, there are many schemes to realize and demonstrate, such as BPF filters, microring resonators, delay interferometers (fiber-based, silicon waveguide based, LiNbO$_3$ waveguide based, PMF loop mirror, etc.), FP etalons, dispersive fibers, arrayed waveguide grating (AWG) and so on. Usually we should cascade two or more different kinds of filters to get better output results. It is very important to choose and optimize the filtering processes to realize desired functions and improve the output performance.

In this chapter, we theoretical and experimental analyzed all-optical signal processing with SOAs and tunable filters where SOAs were regarded as spectrum transformers and tunable filters were used to realize different filtering processes and then different signal processing functions. In section 2, complicated theoretical model for SOA is presented, and many nonlinear effects are taken into consideration, such as carrier heating, spectral hole burning, etc. On the other hand, a theoretical model for optimizing the filtering process is also presented. These two theoretical models are value for any different signal processing functions. In section 3, experimental research on all-optical wavelength conversion is discussed and analyzed. In section 4, experimental results for all-optical logic operation are presented. Finally, multi-channel all-optical regenerative format conversion is experimental investigated in section 5. Some remarks are also given in final conclusions.

2. Theoretical model

In order to represent the generality for different kinds of signal processing functions, we establish a general theoretical model based on SOA's model and filter's model. As shown in Fig.1, a SOA is cascaded with two basic filters: an optical bandpass filter (OBF) and a delay
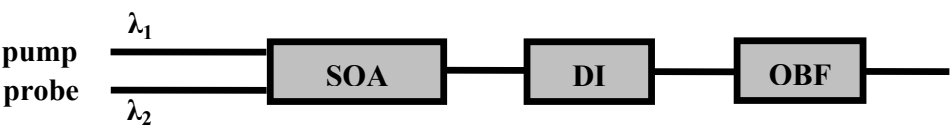

Fig. 1. Schematic diagram for signal processing with SOA and filters

interferometer (DI). These two filters are the most possible to be used to realize signal processing functions. The theoretical model corresponding to Fig. 1 can be exploited to analyze any kinds of signal processing functions. The key point of this model is calculating out the output signal spectrum after the SOA based on a complicated SOA model. Only all kinds of nonlinear effects are taken into account, the accuracy of the output spectrum can be believed. The final output signal spectrum can be analyzed with the help of transmission functions of the cascaded two filters. With iFFT tool, we can get output signal waveform in time domain.

2.1 Theoretical model of SOAs

Based on theoretical models in literatures (Mork & Mark 1995; Mork, et al., 1994; Mork & Mark 1992; Agrawal & Olsson 1989; Mork & Mecozzi 1996), we can derive theoretical model for SOAs in which ultrafast nonlinear effects are taken into account. Firstly, the propagation equation for the input signal in the SOA can be derived as the following equation:

$$\frac{\partial A(z,\tau)}{\partial z} = \left\{ \frac{1}{2}\Gamma g(z,\tau) - \frac{1}{2}\Gamma_2\beta_2(1+i\alpha_2)|A(z,\tau)|^2 - \frac{1}{2}\Gamma\beta_C n_C(z,\tau) - \frac{1}{2}\Gamma\beta_v n_v(z,\tau) - \frac{1}{2}\alpha_{int} \right.$$

$$\left. + \frac{i}{2}[\alpha g_N(z,\tau) + \alpha_{CH}\Delta g_{CH}(z,\tau) + \alpha_{SHB}\Delta g_{SHB}(z,\tau)] \right\} A(z,\tau) \tag{1}$$

In Eq.(1), the first to fifth terms on the right hand side represent the linear gain, two-photon absorption (TPA), FCA in conduction band, FCA in valence band and linear absorption loss respectively. The last three terms represent phase modulation process accompanied with linear gain variation, carrier heating and spectral hole burning, which are corresponding to parameters α, α_{CH} and α_{SHB} respectively.

In order to calculate the gain coefficient, the local carrier densities should be calculated out firstly. The local carrier densities satisfy the following two equations (Mork, et al., 1994):

$$\frac{\partial n_c(z,\tau)}{\partial \tau} = -\frac{n_c(z,\tau) - \bar{n}_c(z,\tau)}{\tau_{1c}} - v_g g(z,\tau)S - n_c(z,\tau)\beta_c v_g S \tag{2}$$

$$\frac{\partial n_v(z,\tau)}{\partial \tau} = -\frac{n_v(z,\tau) - \bar{n}_v(z,\tau)}{\tau_{1v}} - v_g g(z,\tau)S - n_v(z,\tau)\beta_v v_g S \tag{3}$$

The first terms on the right hand sides of Eq. (2)and (3) describe the relaxation process of the electrons and holes to their quasi-equilibrium values $\bar{n}_c(z,\tau)$ and $\bar{n}_v(z,\tau)$, respectively. These relaxation processes are driven by the electron-electron and hole-hole interaction with time constant of τ_{1c}, τ_{1v}. The second terms describe carrier consumption due to stimulated emission, and the last terms corresponding to carrier consumption due to two photon absorption.

In this theoretical model, the gain can be expressed as the following equations:

$$\begin{cases} g(z,\tau) = \dfrac{1}{v_g} a(\omega_0)[n_c(z,\tau) + n_v(z,\tau) - N_0] \\[2mm] g_N(z,\tau) = \dfrac{1}{v_g} a(\omega_0)[n_c^*(z,\tau) + n_v^*(z,\tau) - N_0] \\[2mm] \Delta g_{CH}(z,\tau) = \dfrac{1}{v_g} a(\omega_0)[\overline{n_c} - n_c^*(z,\tau) + \overline{n_v} - n_v^*(z,\tau)] \\[2mm] \Delta g_{SHB}(z,\tau) = \dfrac{1}{v_g} a(\omega_0)[n_c - \overline{n_c} + n_v - \overline{n_v}] \end{cases} \tag{4}$$

where $a(\omega_0)$ is the differential gain coefficient, and N_0 is the transition density of states in optically coupled region. g is total gain dynamics, g_N the gain changes accompanied with carrier density variation due to interband recombination, Δg_{CH} the gain changes due to CH, Δg_{SHB} the gain changes due to SHB.

In order to solve Eqs. (2) ~ (4), $\overline{n}_R(z,\tau)$, $n_R^*(z,\tau)$, $R \in [c,v]$ should be got firstly, and they can be defined as:

$$n_R(z,\tau) = N_0 F(E_{fR}, T_R(z,\tau), E_R) \tag{5}$$

$$n_R^*(z,\tau) = N_0 F(E_{fR}, T_L, E_R) \tag{6}$$

where E_{fc} and E_{fv} are the quasi-Fermi level in the conduction band and the valence band, respectively. T_C and T_V are the temperature of the carriers in the conduction band and the valence band. T_L is the lattice temperature. E_C and E_V are the corresponding transition energies in the conduction band and the valence band. F is the Fermi-Dirac distribution function shown as follows:

$$F(\mu, T, E) = \dfrac{1}{1 + \exp(\dfrac{E - \mu}{k_b T})} \tag{7}$$

To calculate instantaneous carrier temperature (T_R) and quasi-Fermi level (E_{fR}), we need calculate the total electron-hole pair density N and the energy state densities U. The total electron-hole pair density satisfies the following equation:

$$\dfrac{\partial N(z,\tau)}{\partial \tau} = \dfrac{I}{eV} - \dfrac{N}{\tau_s} - v_g g(z,\tau)S + v_g \beta_2 S^2 \tag{8}$$

It should be noted that, $N(z,\tau)$ counts all the electron-hole pairs, including those that are not directly available for the stimulated emission.

The energy state densities satisfy the following two questions:

$$\dfrac{\partial U_c(z,\tau)}{\partial \tau} = \beta_c \hbar \omega_0 n_c S - E_c v_g g(z,\tau)S + E_{2c} v_g \beta_2 S^2 - \dfrac{U_c(z,\tau) - \overline{u}_c(z,\tau)}{\tau_{hc}} \tag{9}$$

$$\dfrac{\partial U_v(z,\tau)}{\partial \tau} = \beta_v \hbar \omega_0 n_v S - E_v v_g g(z,\tau)S + E_{2v} v_g \beta_2 S^2 - \dfrac{U_c(z,\tau) - \overline{u}_c(z,\tau)}{\tau_{hv}} \tag{10}$$

In these equations, the first terms describe the change in energy density due to the stimulated emission. The second terms depict the changes due to FCA and the third terms account for the TPA. The last terms represent the relaxation to equilibrium due to carrier-phonon interactions with time constant of τ_{hc} and τ_{hv}. The equilibrium energy densities are defined as:

$$\overline{U}_C = \frac{1}{V}\sum_k \frac{\hbar k^2}{2m_c^*} F(E_{fc}(z,\tau), T_L(z,\tau), \frac{\hbar k^2}{2m_c^*}) \tag{11}$$

$$\overline{U}_v = \frac{1}{V}\sum_k \frac{\hbar k^2}{2m_v^*} F(E_{fv}(z,\tau), T_L(z,\tau), \frac{\hbar k^2}{2m_v^*}) \tag{12}$$

The total carrier density and total energy density need to be self consistently calculated in each time step. We can calculate the quasi-Fermi level and instantaneous temperature of the electrons in conduction band based on self consistently theory.

$$\begin{cases} N(z,\tau) = \frac{1}{V}\sum_k F(E_{fc}(z,\tau), T_c(z,\tau), \frac{\hbar k^2}{2m_c^*}) \\ U_c(z,\tau) = \frac{1}{V}\sum_k \frac{\hbar k^2}{2m_c^*} F(E_{fc}(z,\tau), T_c(z,\tau), \frac{\hbar k^2}{2m_c^*}) \end{cases} \tag{13}$$

Similarly, we can also obtain the instantaneous Fermi levels and temperatures in the valence band.

$$\begin{cases} N(z,\tau) = \frac{2}{V}\sum_k F(E_{fv}(z,\tau), T_v(z,\tau), \frac{\hbar k^2}{2m_v^*}) \\ U_v(z,\tau) = \frac{2}{V}\sum_k \frac{\hbar k^2}{2m_v^*} F(E_{fv}(z,\tau), T_v(z,\tau), \frac{\hbar k^2}{2m_v^*}) \end{cases} \tag{14}$$

It should be noted that, the factor of 2 on the right hand of Eq.(14) is observed, because we consider two sub-bands in valence band including heavy hole band and light hole band.
Using Eqs(1-14),we can numerically simulate the dynamics characterization in SOA active region and the signal propagation.

2.2 Theoretical model for filtering

OBFs and DIs are typical filters for all-optical signal processing, especially in ultrahigh speed operation scheme. The transmission function of the BPF and the DI can be described as the following two expressions.

$$\begin{cases} F_1(\omega) = \frac{1}{2}[\exp(i\phi) + \exp(i2\pi\tau\omega)] \\ F_2(\omega) = \exp[-2\ln 2 \cdot (\frac{\omega - \omega_f}{B_0})^2] \end{cases} \tag{15}$$

where F_1 and F_2 are the transmission function of DI and band-pass filters, respectively. ϕ is the phase difference between two arms of the DI, τ is the time delay of two arms of the DI. ω_f is the central angle frequency of the BPF, B_0 is 3 dB bandwidth of the BPF.

The optical field after SOA can be described as:

$$E_{out}(t) = \sqrt{P_{out}} \exp[i(\omega_0 t + \Phi_{NL}(t))] \tag{16}$$

Based on Fast Fourier Transformer (FFT), the optical spectrum of the output signal after the SOA can be obtained as

$$E_{out}(\omega) = FFT[E_{out}(t)] \tag{17}$$

After optical filtering process, the optical spectrum of the output signals after the two cascaded filters can be described as:

$$E_{opt}(\omega) = E_o(\omega) \cdot F_1(\omega) \cdot F_2(\omega) \tag{18}$$

Then, based on inverse Fast Fourier Transformer (iFFT), the output signal waveform in time domain can be calculated out.

$$P_{opt}(t) = \left| F^{-1}[E_{opt}(\omega)] \right|^2 \tag{19}$$

It should be noted that sometimes we should exploit more filters to optimize the output performance, but, the analytical process is identical, adding the transmission function of the new filter in Eq. 17 can get the correct output results.

2.3 Applications in all-optical signal processing

For some applications, the configuration and mechanism are fixed and known to us, we can analyze the output performance based on above theoretical model. The analytical process based on the above SOA model and filter model can be illustrated as the following flow diagram.

As shown in Fig.2, based on above SOA theoretical model, we can get output signal waveforms in time domain from SOA and phase variation information is also included in the output signal filed. Using FFT tool, we can calculate out the signal spectra. Combing with the filter model iFFT tool, we can simulate out the output signal field. We can optimize the SOA parameters or filter parameters to improve the output performance. This process can be used to optimize the SOA structure and filter shape for special applications.

On the other hand, we can also use the above theoretical model to explore some novel schemes for special signal processing functions. The analytical process can be illustrated as following flow diagram. As shown in Fig.3, for special signal processing functions, input signal and output signal are fixed and known to us, their spectra can be calculated out based on FFT tool, so the transmission functions of the potential schemes can be determined by input spectra and output spectra. Usually, the spectrum transformation process of the SOA is fixed and can be determined by the above SOA model. Using some iteration algorithms, the filtering process and related filters can be optimized.
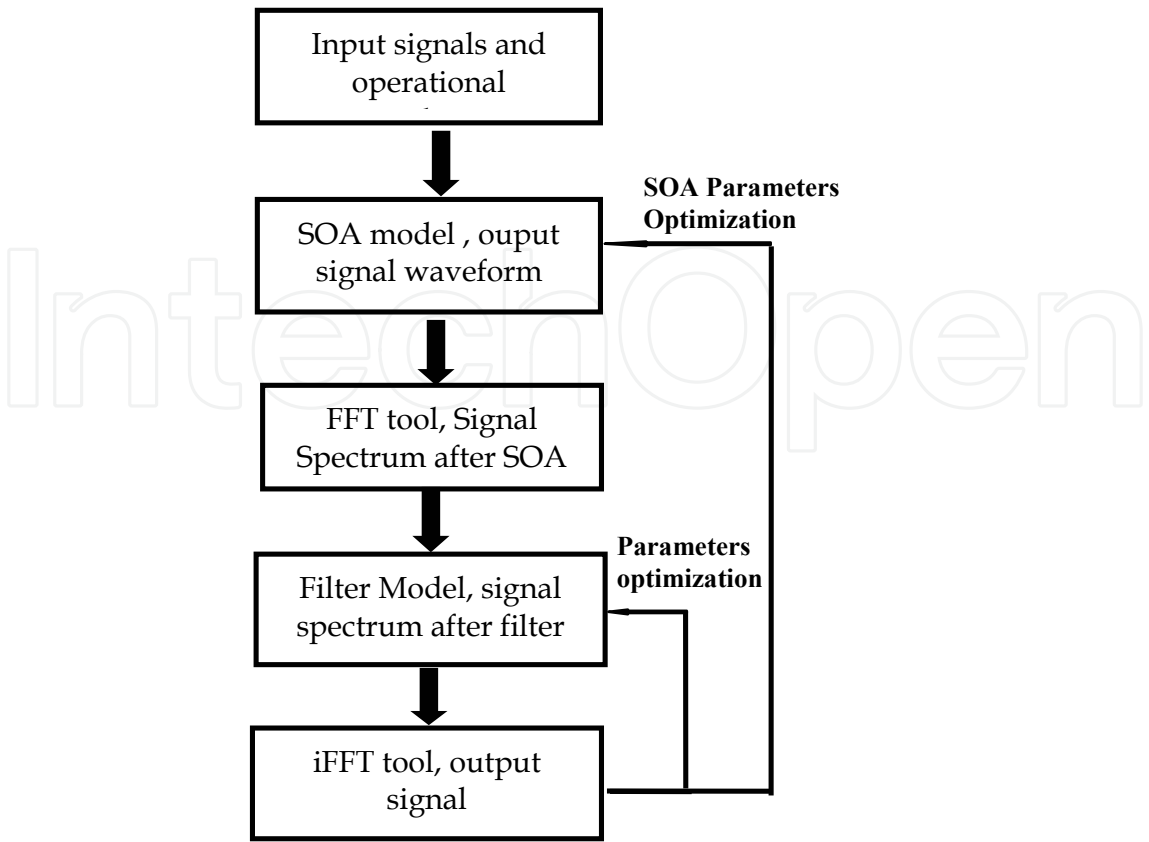
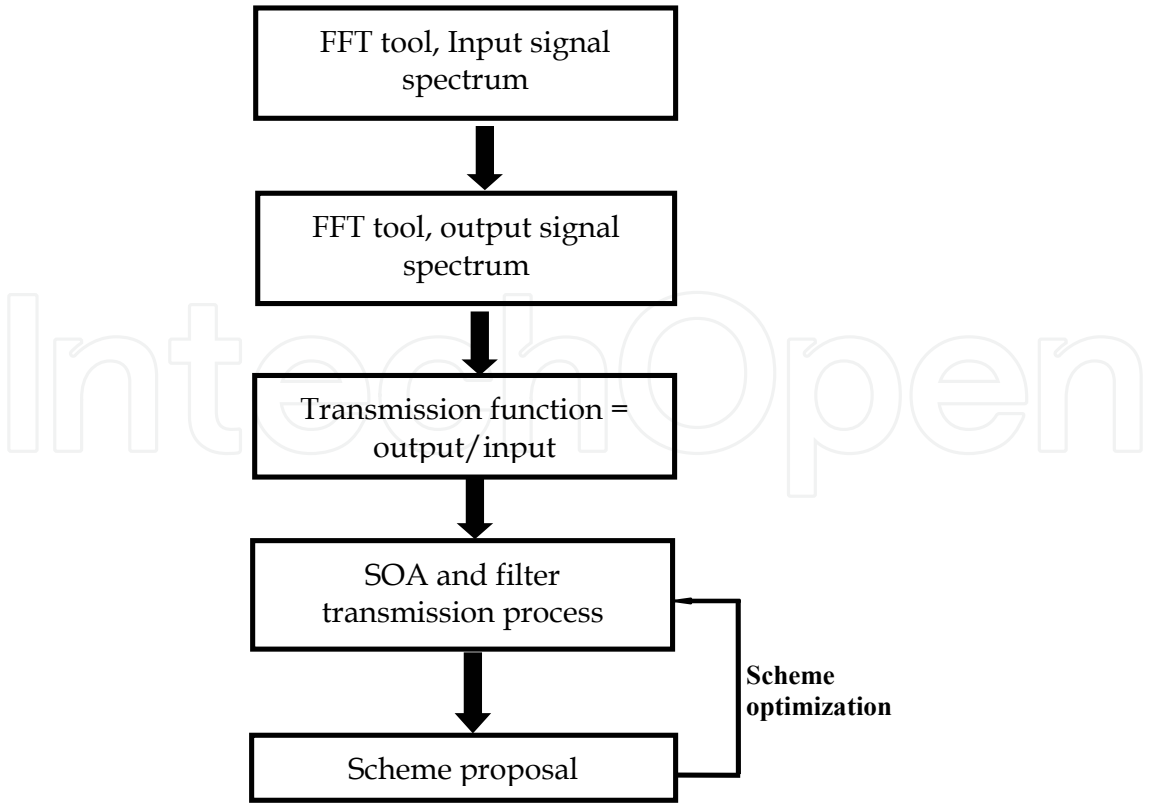Fig. 2. Analytical process for all-optical signal processing schemes with fixed configurations

Fig. 3. Analytical process diagram for exploring novel schemes

3. All-optical wavelength conversion with SOAs and filters

All-optical wavelength conversion can be regarded as the most important signal processing function because it is the basis of other signal processing functions. In this section, inverted and non-inverted wavelength conversion at 40Gb/s based on different filter detuning were investigated firstly (Dong et al., 2008), then, experimental results on 80Gb/s wavelength conversion and related filtering optimization process are discussed (Huang et al., 2009).

3.1 Bi-polarity wavelength conversion for RZ format at 40Gb/s

Fig. 4 shows the schematic diagram of both inverted and non-inverted wavelength conversion (Dong et al., 2008). A CW probe signal and a data signal with RZ format are launched into an SOA. The following OBF has some detuning to the probe signal with the central wavelength $\lambda_c + \Delta\lambda_{det}$, where $\Delta\lambda_{det}$ is the detuning value from probe wavelength at λ_c. The input 40Gb/s RZ signal will induce transient nonlinear phase shifts and intensity modulation to the probe signal via cross phase modulation (XPM) and cross gain modulation (XGM) in the SOA. The nonlinear phase shifts will result in a chirped converted signal with the broadened spectrum. The leading edges of the converted probe light are red-shifted, whereas the trailing edges are blue-shifted. Whether the output converted signal is inverted or non-inverted depends on the detuning value.
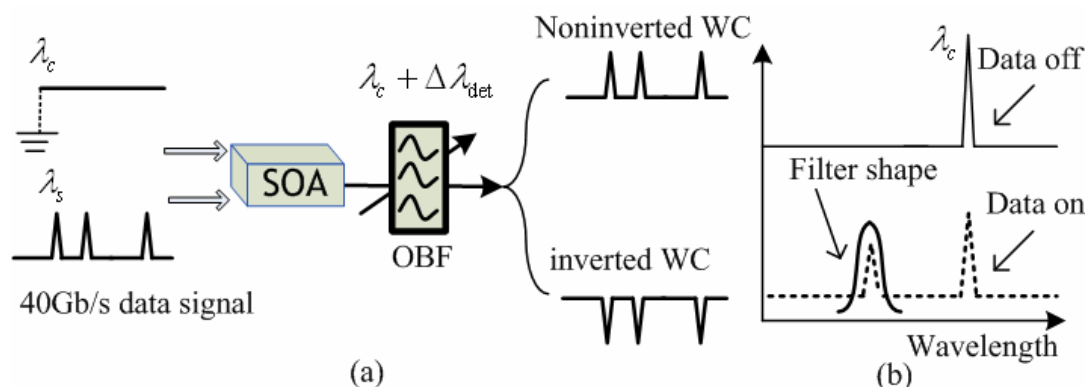

Fig. 4. (a) Operation principle of the bi-polarity wavelength conversion, (b) variation of probe spectrum in the non-inverted wavelength conversion

On the one hand, the wavelength shift of the chirped probe occurs only in the leading/trailing edges of input RZ signals. When the data signal is mark, the probe spectrum will be broadened with sideband energy. If the OBF is detuned far away from the probe wavelength so as to select the sideband energy at $\lambda_c + \Delta\lambda_{det}$, the OBF output will be mark. When the data signal is space, there is no instantaneous frequency shift, and then the OBF output is space, as shown in Fig. 4(b). Therefore, the converted signal will keep in-phase to the input RZ signal. That is non-inverted wavelength conversion.

On the other hand, the XGM will result in the inverted wavelength conversion with relatively slow recovery without the OBF detuning. However, the amplitude recovery can be accelerated and the pattern effects can be eliminated if the OBF is slightly blue shifted. The reason can be explained in Fig. 5. The dotted and dashed lines are the SOA gain and chirp, respectively. When the pulse starts at point A, the SOA carrier depletes and the gain reaches the pit at point B. In time slot from A to B, the probe experiences red chirp and the blue shifted OBF attenuates the probe power. After the pulse duration stops, the gain starts

to recover slowly. Assume that the probe signal gets its maximum blue chirp at point C. After point C, the chirp decreases toward zero, then the blue shifted OBF decreases the transmittance. But the gain recovery is going on. Therefore, the blue shifted OBF can balance the power of blue chirped component and the probe power during gain recovery. As a result, the net power at the OBF output is approximately constant (see time slot from C to D). If the SOA and the OBF are treated as a whole system, the amplitude recovery of the system is much faster than the SOA gain. The fast amplitude recovery technique is also suitable for NRZ format. The detail explanation can be found in reference (Liu et al., 2006).
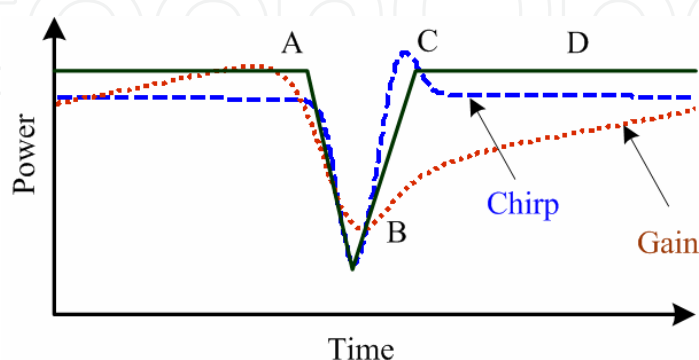
Fig. 5. Principle of accelerating the amplitude recovery.

The experimental setup for bi-polarity wavelength conversion is shown in Fig. 6. Tunable laser diode (LD1) generates a CW probe light at 1557.32nm with the power of 0dBm. Tunable LD2 generates another light source at 1563.5nm, which is modulated by two LiNbO$_3$ Modulators at 40Gb/s to form a 2^{31}-1 RZ pseudo random binary sequence (PRBS) signal, then an erbium-doped fiber amplifier (EDFA) and an attenuator (ATT) are used to fix the RZ output average power at -1.8dBm. The 40Gb/s RZ signal with 8ps-wide pulses is combined with the probe light, and launched into the SOA. The SOA (Kamelian NL-SOA) is biased at 200mA, and its 90%~10% recovery time, defined as the time needed for the gain compression to recover from 90% to 10% of the initial compression, is about 60ps, which is longer than one bit period. The small signal gain@1550nm is 22dB. A tunable OBF1 with bandwidth of 0.32nm follows the SOA. The OBF1 has somewhat detuning to the probe signal to obtain high speed wavelength conversion. Another EDFA and an OBF with 1nm
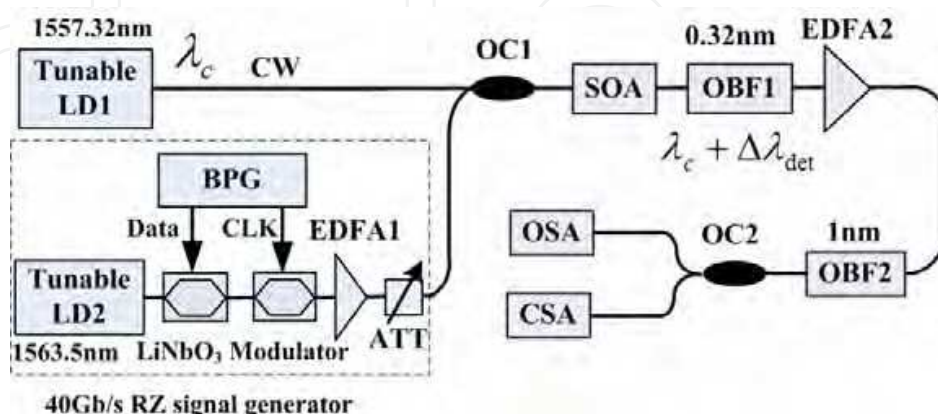

Fig. 6. Experimental setup for bi-polarity wavelength converters at 40Gb/s. BPG: bit pattern generator; ATT: attenuator; OC: optical coupler; OSA: optical spectrum analyzer; CSA: communication signal analyzer.

bandwidth are used to amplify the converted signal power and eliminate the crosstalk. Finally, the optical spectrum analyzer (OSA) and communication signal analyzer (CSA) are used to observe the optical spectrum and waveform of the converted signal.

Fig. 7 shows the experimental results of both inverted and non-inverted wavelength conversion. The left column is the captured waveforms whose time scale is 52ps/div, and the right column is the corresponding eye diagrams whose time scale is 20ps/div. Fig. 7(i) shows the waveform of input 40Gb/s RZ signal. When the OBF1 detuning is -0.3nm (blue shifted) and +0.4nm (red shifted) respectively, the non-inverted wavelength conversion is observed in Fig. 7(ii) and (iv). Good eye diagram is shown in Fig. 7(ii) while some pattern effects occur in Fig. 7(iv). We can see the consecutive marks ①, ②, ③ show a decreasing amplitude. When the OBF1 is slightly blue shifted by 0.1nm, the output waveform becomes inverted and no pattern effects occur, shown in Fig. 7(iii). When the OBF1 has the same central wavelength to the probe carrier, the output waveform has very serious pattern effects, shown in Fig. 7(v). Therefore a slightly blue shifted OBF can accelerate the amplitude recovery in the inverted wavelength conversion.
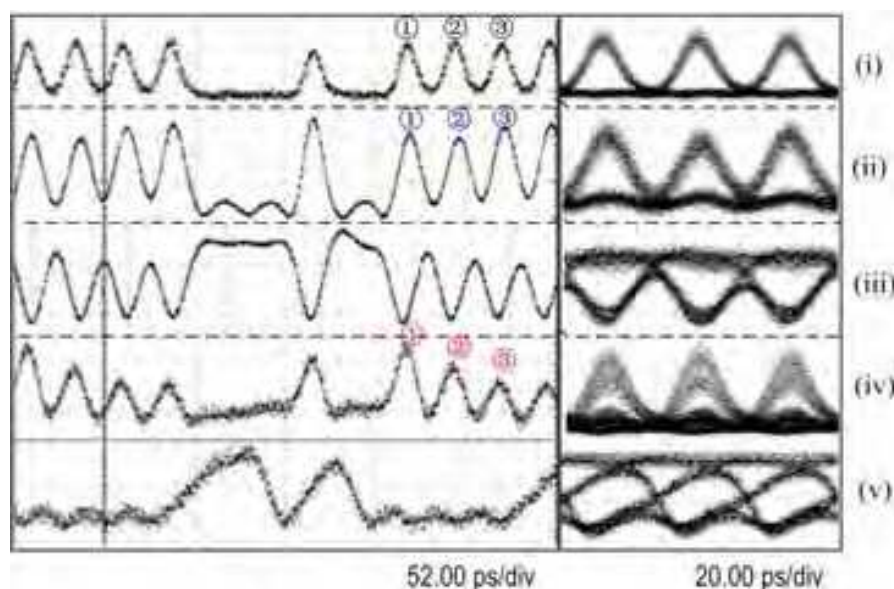

Fig. 7. Waveforms of converted signal with different detuning, (i) the input RZ waveform, (ii)-(v) are the output waveforms of converted signal when the OBF1detuning is -0.3nm, -0.1nm, +0.4nm, and 0nm, respectively. The left column and right column are the captured waveforms and eye diagrams.

The experimental results can be explained from the spectrum. Fig. 8 shows the spectra of converted signal when the OBF1 is detuned. The probe spectra before and after the SOA are shown in Fig. 8(a). At the SOA output, the probe spectrum is broadened asymmetrically due to the XPM. The output spectra of converted signals are shown in Fig. 8(b)-(e) corresponding to the OBF1 detuning -0.3nm, -0.1nm, +0.4nm, and 0nm, respectively. In Fig. 8(b), the blue sideband of converted signal becomes dominant with the assistance of the blue shifted OBF1, therefore good eye diagram could be observed. While in Fig. 8(d), the OBF1 cannot suppress the probe carrier. The crosstalk between red sideband peak and probe carrier will result in the pattern effects in time domain. In Fig. 8(b) and (d), the OBF1 detuning is different for achieving the best non-inverted wavelength conversion because of the asymmetric probe spectrum at the SOA output. Besides, the negative slope of OBF1 is

larger than the positive slope, so the blue shifted OBF is easy to suppress the probe carrier, but red shifted OBF is not. In Fig. 8(c), the probe carrier keeps dominant, so the output waveform becomes inverted.

The non-inverted wavelength conversion with blue shifted OBF shows better performance than red shifted OBF. This can be explained with the chirp characteristics. Fig. 9(a) shows the input RZ signal with four consecutive bits "1", and Fig. 9(b) shows the probe phase variation at the SOA output. One can see that the phase increases fast in the leading edge, which corresponds to carrier depletion. However the phase decreases slowly in the trailing edge, which results from the carrier recovery. Fig. 9(c) shows the probe chirp, which is the first order derivative of the phase variation by contrariety. With consecutive "1" pulses injection, the carrier depletion decreases, then the red peak chirp decreases as well. This leads to the decreasing amplitude of the converted pluses by means of the red OBF transfer function (see ①, ②, ③ of the red OBF), and the converted pulses show serious pattern effects. On the other hand, one notices that the blue peak chirp increases very slowly, and remains constant approximately. This results from the similar carrier recovery under consecutive "1" pulses injection. By means of the blue OBF transfer function, the amplitude of converted pulses remains constant (see ①, ②, ③ of the blue OBF). Therefore, the non-inverted wavelength conversion performance is better with blue shifted OBF than with red shifted OBF.
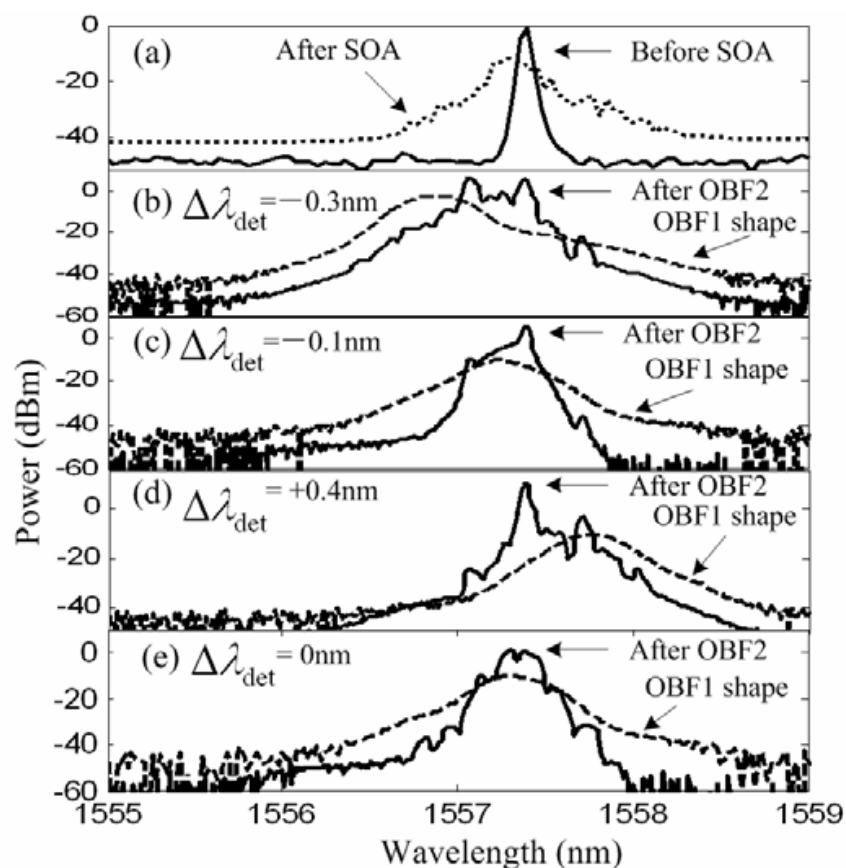

Fig. 8. Spectra of converted signal with different detuning, (a) the probe spectrum before and after SOA, (b)-(e) are the output spectra of converted signal when the OBF1 detuning is -0.3nm, -0.1nm, +0.4nm, and 0nm, respectively.
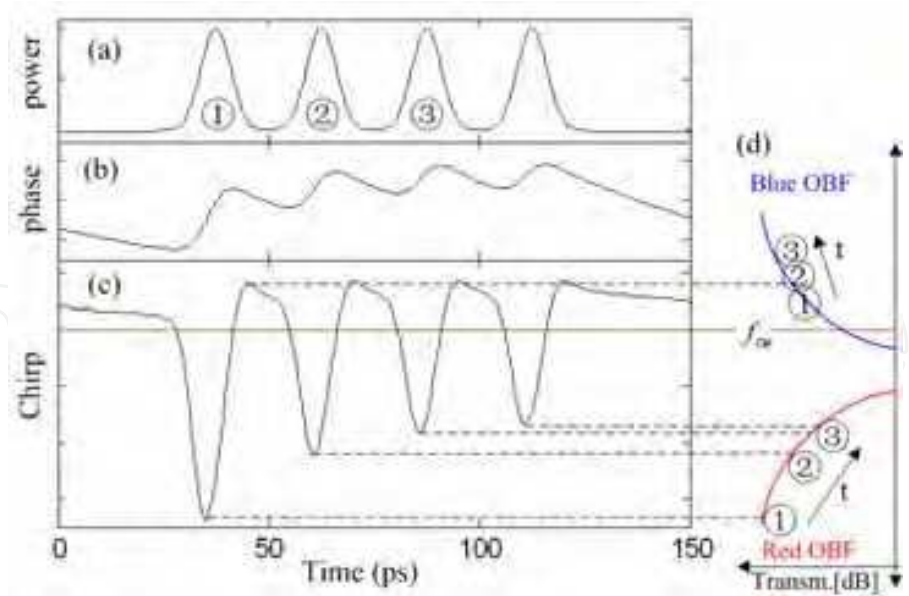
Fig. 9. Comparison of blue shifted OBF and red shifted OBF by frequency-amplitude conversion at the OBF slopes, (a) consecutive "1" pulses, (b) phase evolution, (c) chirp evolution, (d) frequency-amplitude conversion.

The wavelength tunability is further investigated in our experiment. For ease of discussion, we only adjust the wavelength of tunable LD2. We investigate the output extinction ratio (ER) under the optimal OBF1 detuning, as shown in Fig. 10. The output ER fluctuates around 7dB in the whole C-band (1528-1563nm), except the near region of RZ wavelength. The inset of Fig. 10 shows the SOA amplified spontaneous emission (ASE) spectrum, which reveals that the SOA gain is low at the shorter wavelength. Therefore the ER decreases at shorter wavelength. Our experiment scheme cannot complete the wavelength conversion of the same wavelength since the OBF cannot separate the probe and signal channels at the same wavelength.
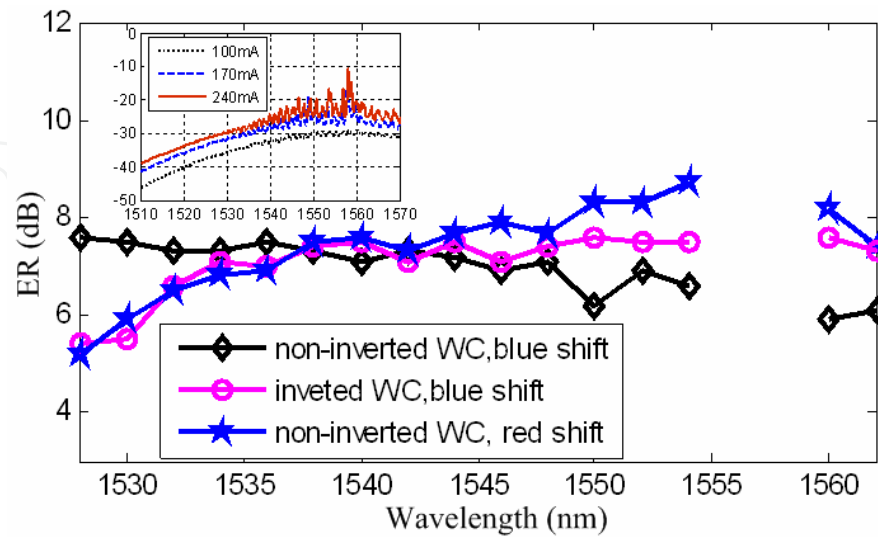
Fig. 10. Output ER as a function of the input signal wavelength when the OBF1 detuning is -0.3nm, -0.1nm, and +0.4nm, respectively. The inset is the SOA ASE spectra at different bias currents.

From Fig. 10, we can see that the output ER is not very high in the three kinds of wavelength converters. The reasons resulting in low ER are quite different between inverted wavelength conversion and non-inverted wavelength conversion. For non-inverted wavelength conversion, the OBF1 does not have a sharp slope, which could not separate the sideband signal from the probe spectrum completely, as shown in Fig. 8(b) and (d). Therefore, the crosstalk between the sideband signal and the probe carrier will degrade the output ER. For inverted wavelength conversion, we need ultrashort pulse injection to enhance the T-XPM effect and to generate large chirp of the probe signal. However, the 8ps-wide input pulses are not narrow enough to obtain inverted wavelength conversion with large ER. We believe the output ER could be improved if the OBF slope is optimized and the input RZ pulses are compressed as narrow as possible.

3.2 80Gb/s wavelength conversion with SOA and cascaded filters
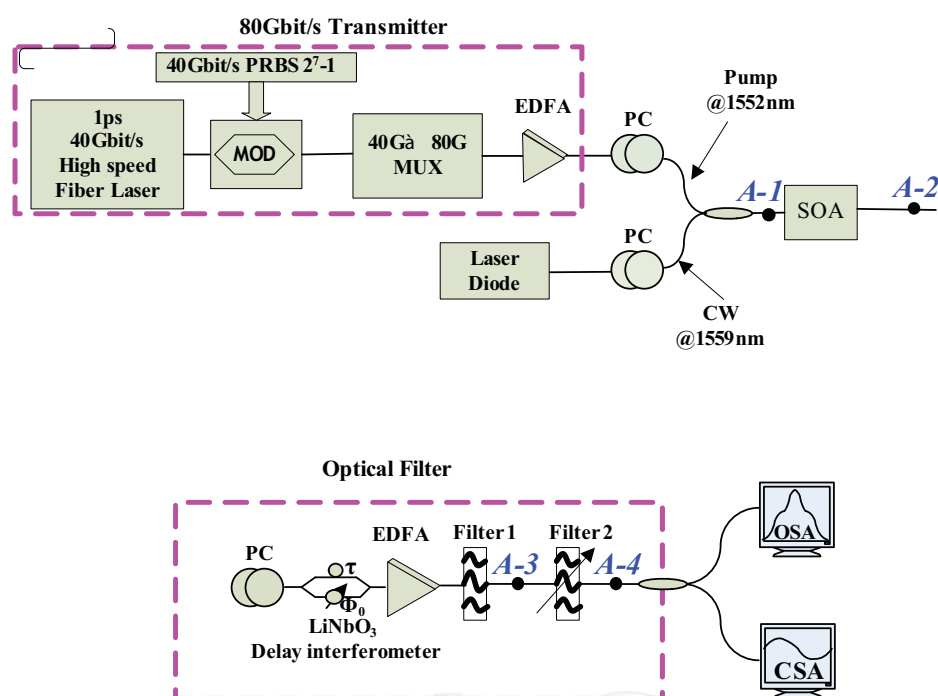
Fig. 11. Experimental setup for 80Gb/s wavelength conversion with SOA and cascaded filters: PC: Polarization controller, EDFA: Erbium-doped fiber amplifier, OSA: optical spectrum analyzer; CSA: communication signal analyzer.

The experimental setup is shown in Fig.11 (Huang et al., 2009). A 40GHZ 1.0-ps wide (FWHM) optical pulse is modulated by an external amplitude modulator (MOD) at 40Gbit/s to generate a 2^7-1 RZ-PRBS signal. This data stream is then optical time multiplexed (MUX) to 80Gbit/s. After amplification, the average optical power of the 80Gbit/s data stream is 4.8mW and the continuous wave (CW) probe signal is 3mW. After the polarization controller, the 80Gbit/s signal is combined with the CW probe and fed into an SOA via 3 dB coupler. As shown in Fig.12, the cascaded filtering model is consisted of a 3.125 ps delay LiNbO$_3$-DI, an optical band-pass filter 1 with bandwidth of 3 nm and the tunable optical band-pass filter 2 with bandwidth of 1 nm which is detuned 1.2 nm to the blue side of the probe carrier wavelength. An inverted 80Gbit/s signal can be obtain at the output of the SOA. The converted signal is subsequently injected into the LiNbO$_3$ DI, where

the inverted signal is converted into a non-inverted signal. At the output of the tunable optical band pass filter 2, the non-inverted probe signal is monitored by using an optical sampling scope; the optical spectrum is analyzed by using an optical spectrum analyzer (OSA) with a resolution of 0.050 nm, simultaneously. In our experimental setup, the SOA is biased at 250mA.

It should be noted that, the sampling frequency of the OSA used in our experiment is 40GHz, while the data stream is modulated at 80 Gb/s. Thus the short pulse monitored by the OSA is broadened. However, we are still able to distinguish the eye opening and ER of the output waveform which are shown in Fig.13 (b), (c), (d).
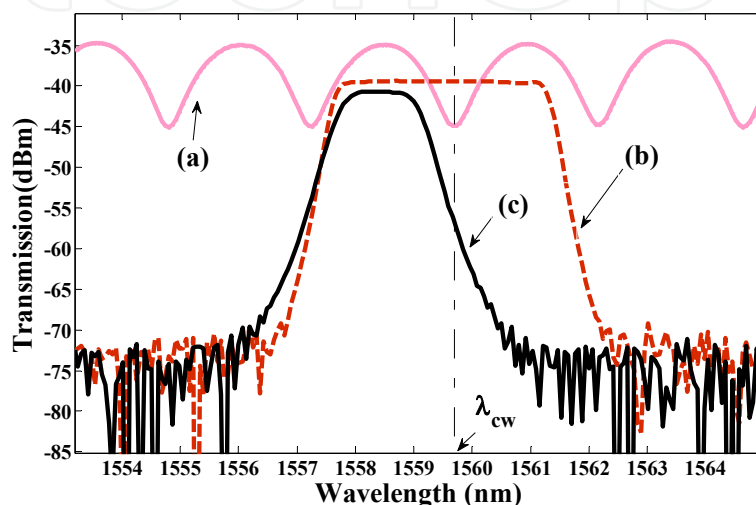
Fig. 12. Transmission spectra the DI (a-1), the band pass filter 1(a-2), the band pass filter2 (a-3).

The operation principle for optical spectrum filtering base on SOA is described as follows. An ultra-fast pulse-stream is combined with a CW probe light and launched into the SOA. The pump signal will induce nonlinear phase shift to the probe signal via T-XPM in the SOA, As a result, the spectrum of the probe signal is broadened. To obtain the high output quality, we optimize the spectrum filter using the $LiNbO_3$ DI and band-pass filters. As seen curve (a) in Fig.12, the "notch" characteristic of $LiNbO_3$ DI is clearly visible. An important feature to be noted is that for the non-inverted output, the wavelength of the notch is set to be the center wavelength of the converted probe signal, ensuring a high attenuation of DC component corresponding to the "1"level in the inverted signal and a larger transmittance of the "0"level.On the other hand, the $LiNbO_3$ DI modifies the spectrum of the output probe of SOA. The central wavelength of the filter 1 is fixed at carrier wavelength of the probe signal .Thus, the pump signal is suppressed and the power ratio of the probe and pump signal is about 30dB (seen in Fig.13 (A-3)).Another low-noise EDFA 2 is applied to amplify the output signal. Then, we use the filter 2 to extract out the component at the central wavelength $\lambda_C + \Delta\lambda$, where λ_C is the central wavelength of the probe signal, $\Delta\lambda$ is the detuning value from λ_C. In this experiment, probe wavelength λ_C is 1559.89nm, and the wavelength detuning $\Delta\lambda$ is -1.2nm.

Fig.13 (a) depicts the optical spectrum measurement at the different position of the experimental setup.Fig.13 (b-d) shows the measured eye diagrams. Fig.13 (b) is the input pump signal at 1541nm, Fig.13(c) shows the eye diagram of the output signal after the OBF1, and Fig.13 (d) depicts output signal after OBF2. They all show good eye-opening

performance, the ER of input pump signal is 13.529dB, while the ER of output signal after the BPF 1 is only 3.291dB, and the ER of output signal after the OBF 2 is as high as 20.00dB.
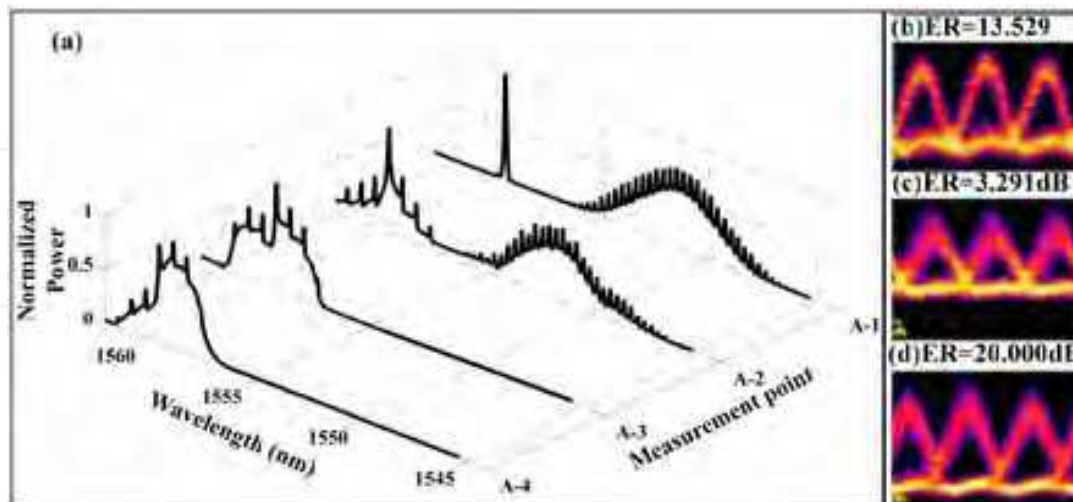

Fig. 13. Experimental results for 80Gb/s wavelength conversion (a) the optical spectrum measurement at different position corresponding to Fig.11; Eye diagram for (b) input pump signal at 1552nm, (c) output probe signal after OBF 1, (d) output probe signal after OBF 2

For wavelength conversion with SOAs, XGM, XPM, FWM and Transient XPM effects can all be exploited. However, for different operation conditions, one main effect dominates over other effects which maybe improve or degrade the output signal performance. Therefore, optimization of SOA parameters, filtering parameters and operational conditions is very important to get better output performance, and this optimization process can be achieved based on theoretical model presented in section 2.

4. All-Optical logic operation with SOAs and filters

In this section, we will focus on experimental study for all-optical logic operation based on SOAs and filters. Three schemes for all-optical logic operation were introduced. Firstly, All-optical logic AND gate at 40Gb/s based on XGM in cascaded SOAs was presented (Xu et al., 2007), and operation condition and output performance were analyzed. Secondly, based on single SOA and different filtering processing, five different logic gates were demonstrated (Dong(b) et al., 2007; Dong et al., 2008; Wang et al., 2007), different nonlinear effects such as XGM, FWM, Transient XPM are exploited in different logic gates respectively. Thirdly, a flexible scheme for all-optical minterms generation was proposed and demonstrated (Xu(a) et al., 2008; Xu(b) et al., 2008). Based on DI and XGM of SOAs, all-optical minterms for two input signals and three input signals were realized respectively.

4.1 All-optical logic AND gate based on cascaded SOAs

It is known that the logic function of inverted wavelength conversion can be written as $\overline{A} \cdot B$ given that data signal A and B are used as pump and probe light respectively. Particularly, it degenerates into a NOT gate when a continuous-wave (CW) serves as the probe light. Therefore, AND gate can be realized by cascading two sets of SOA and filter and configuring the first one as a NOT gate, i.e. $A \cdot B = \left(\overline{\overline{A}} \right) \cdot B$ (Zhang et al., 2004).
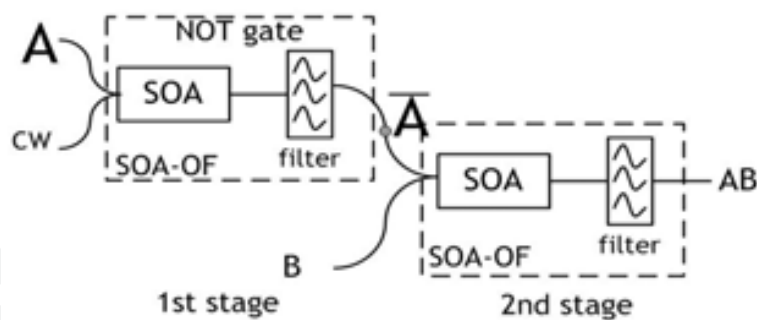
Fig. 14. Schematic diagram for all-optical logic AND gate with cascaded SOAs

As shown in Fig. 14 (Xu et al., 2007), a continuous wave (CW) beam is used as an intermediate wavelength connecting two stages. As probe light at the first stage, it is converted into the negated signal of data A at the output of first stage and serves as pump light at the second stage. Note that the optical filter mentioned above particularly refers to the one who effectively reshapes the spectrum of the modulated probe light. If pump wavelength can not be blocked by such OF, additional optical filter should be used to set the pump and probe wavelength apart.

The experimental setup for the ultrafast AND gate is shown in Fig. 15. In this experiment, three wavelengths generated by LD1, LD2, LD3 are 1560nm(λ_1), 1549.32nm(λ_2) and 1555.75nm(λ_C) respectively. λ_1, λ_2 are modulated by Transmitter simultaneously with 2^7-1 pseudo-random binary sequence (PRBS) RZ data streams at 40Gb/s. The duty cycle of these RZ pulses is 33%. Two wavelengths are separated by a demultiplexer (DMUX) and the optical delay line (ODL) is used to synchronize the input data sequences at the second stage. Thus, two quasi-independent data signals at λ_1 and λ_2 are obtained at the input of SOAs. λ_C is used as intermediate wavelength. The time delay of DI is 25ps which equals to the single bit period of 40Gb/s data rate. The optical BPF following the DI is used to extract the probe light. The filtered probe light is amplified before coupled into the second SOA. The 3dB bandwidth of the Tunable BPF is 0.32nm. The average optical power measured at the input of SOA1 are 7.93dBm(λ_1) and 5.92dBm(λ_2), while 3.10dBm(λ_2) and -17.92dBm (λ_C) at the
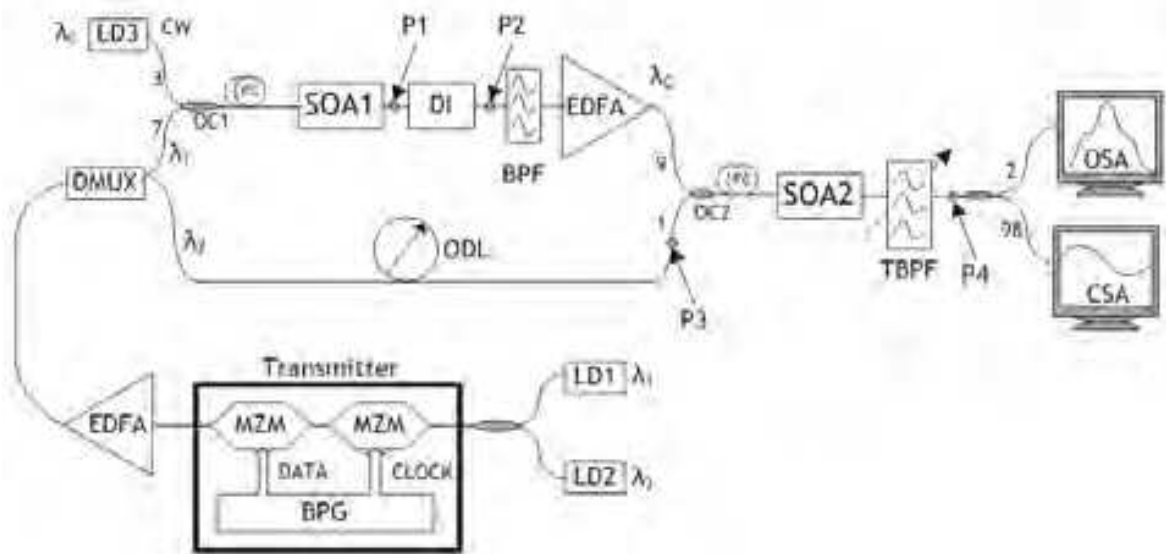

Fig. 15. Experimental setup for all-optical logic AND gate at 40Gb/s with cascaded SOAs

input of SOA2. AND logic results can be achieved through properly tuning the notches of DI and the center wavelength of tunable BPF. In our experiment, the transmission spectrum of the DI can be tuned by adjusting the operational temperature of DI.

Fig. 16 shows the AND logic results (R6) of data signal R7 and R5. R3 is the negated signal of R7, which is NRZ format due to the equivalency between the time delay of DI and the single bit period. The ER of measure AND results is 8.8dB. The bottom trace shows the eye diagram of derived AND results which display open and clear eyes. The QF of the measured eyes is 6.3.
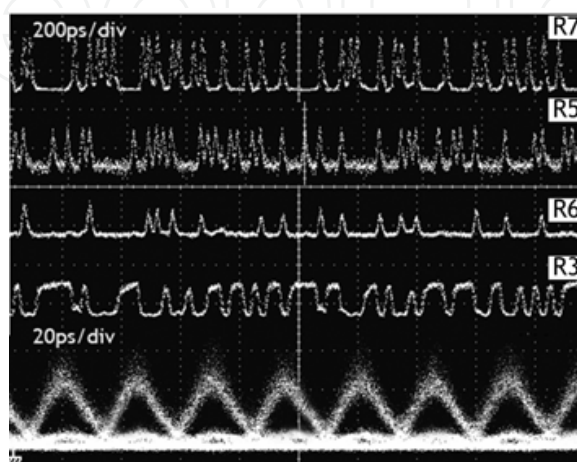
Fig. 16. Output experimental results for all-optical logic AND gate

It should be noted the the SOA1 is a slow recovery bulk material SOA which carrier recovery time is about 500ps. In this SOA, XPM effect is very strong which dominate the output performance. The DI is used to demodulate the phase modulation process, the time delay equals to the bit period, therefore, RZ input signal is wavelength converted to a NRZ signal. The SOA2 is a fast recovery ultrafast SOA which carrier recovery time is about 60ps. The followed the narrow bandpass filter is detuning from the signal B, the detuning process can be optimized to get the best output performance according to the theoretical model in section 2 and analysis of accelarating mechanism in section 3. On the other hand, the most important factor for good AND results is the extinction ratio of the converted signal from stage 1. If we want to improve the output performance or increase the operation speed, the parameters of SOAs and filtering processes should be optimized.

4.2 Configurable all-optical logic gates based on single SOA and tunable filter

In this subsection, we propose and experimentally demonstrate reconfigurable all-optical logic gates based on various nonlinearities in single SOA (Dong(b) et al., 2007; Dong et al., 2008). The operation principle of the configurable logic gates is described in Fig. 17. Data A and B are the data signals to be processed, whose wavelengths are λ_A and λ_B, respectively. The probe signal is a CW at wavelength λ_C, which will be gain- and phase-modulated by the data signals through the SOA. Thus the output optical spectrum of the probe signal will be broadened. Different logic gates can be realized at different OBF setting.

When both data signals are presented in the SOA, the conjugated light is generated due to FWM effect. The converted signal can be optically filtered out to implement AND logic. When either data A or B, or both are presented, the probe signal is gain-modulated with polarity-inverted output, which is logic NOR gate. Whereas, the slow gain recovery of SOA
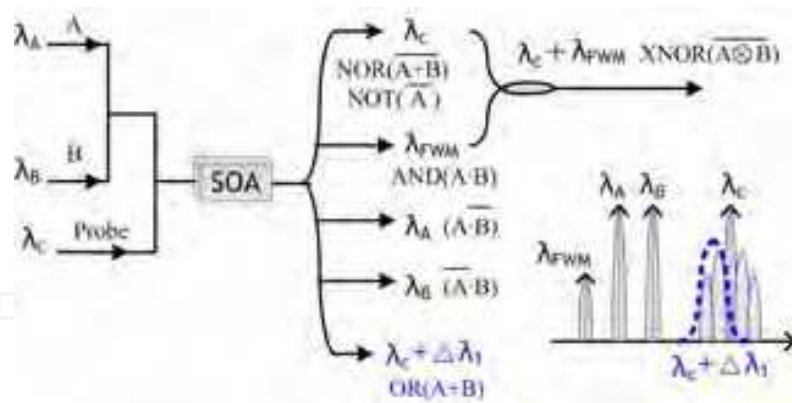
Fig. 17. Illustration of operational principle of the configurable logic gates

degrades the output logic with serious pattern effects. In order to accelerate the SOA gain recovery, the blue shifted OBF with small detuning to the probe carrier is necessary. On the other hand, when the OBF is blue shifted by properly large detuning (i.e., $\lambda_c + \Delta\lambda_1$), the OBF is used to reject the probe carrier and select the blue-shifted spectrum. Either data *A* or *B* or both launched into the SOA will induce blue shifted spectrum, which fits in the OBF passband. If both data signals are absent, the OBF will block the probe carrier. Therefore the output is logic OR gate, which is based on the principle of SOA T-XPM. The XNOR can be obtained by coupling the AND output and NOR output with proper power equalization. The NOR logic gate can be simply changed to NOT logic, merely turning off one data signal.
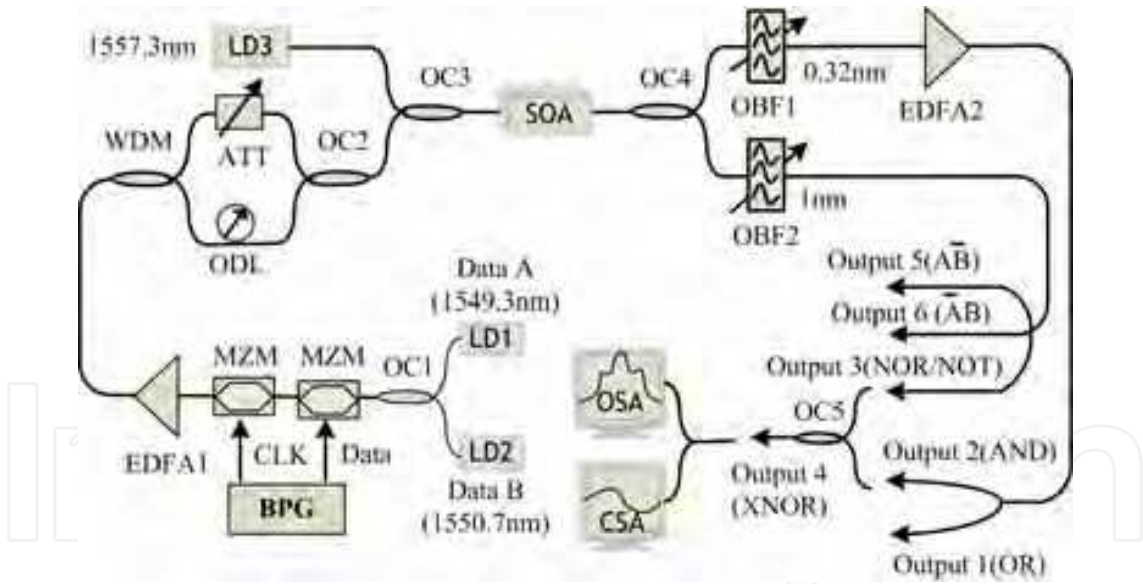
Fig. 18. Experimental setup of the configurable logic gates

The experimental setup for configurable logic gates are described in Fig. 18. The wavelengths of three CW beams generated by LD1, LD2, and LD3 are 1549.3nm (λ_A), 1550.7nm (λ_B), and 1557.3nm (λ_C), respectively. The data signals (λ_A and λ_B) are modulated by two Mach-Zehnder Modulators (MZMs) at 40Gb/s to form $2^{31}-1$ return-to-zero (RZ) pseudo random binary sequence (PRBS) signals. The duty cycle of these RZ pulses is 33%. Two data signals will be separated by the wavelength division multiplexer (WDM) and one of them is delayed for several bits by an optical delay line (ODL), therefore, two data signals with different data pattern are obtained. The employed SOA is the same to that of Fig. 6. A

tunable narrow OBF1 with 0.32nm bandwidth is used to filter the OR logic and AND logic. Another 1nm-bandwidth tunable OBF2 is used to filter the probe signal with NOR/NOT output, or filter the data A with $A\overline{B}$ output, or filter data B with $\overline{A}B$ output. Both $A\overline{B}$ and $\overline{A}B$ should be obtained with large power contrast between data A and B. EDFA2 is used to amplify the AND power, and the coupler (OC5) can combine it with NOR power to realize XNOR logic. Finally, the optical spectrum analyzer (OSA) and communication signal analyzer (CSA) are used to observe the optical spectrum and waveform of the converted signal.
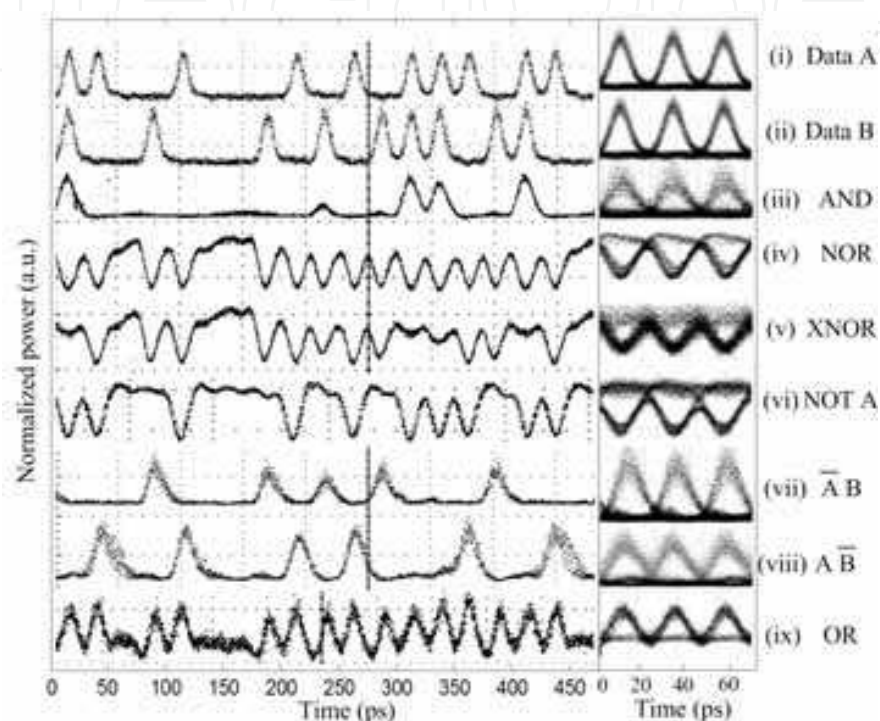
Fig. 19. Output waveforms for different logic gates, (i) and (ii) are input data signals, (iii)-(ix) are logic AND, NOR, XNOR, NOT, $\overline{A}B$, $A\overline{B}$, and OR, respectively.

The input data A and B before entering the SOA are shown in Fig. 19(i) and (ii), respectively. Both waveforms have a peak power of 2.6mW with extinction ratio (ER) over 13dB. The probe signal has a power of 0.6mW. The conjugated light appears at 1548nm at the SOA output. The conjugated light is filtered out by OBF1 and amplified by EDFA2, then the output signal is the logic AND with good eye pattern, as shown in Fig. 19(iii). The output ER is 8.04. In fact, the input probe signal has additional function to accelerate gain recovery speed of SOA and eliminate pattern dependent distortions. When the central wavelength of OBF2 is blue-shifted by 0.1nm with respect to the probe wavelength, the output signal is NOR logic, as shown in Fig. 19(iv). The ER of NOR logic operation is 10dB. The AND output has a low power level due to low conversion efficiency of FWM, while the NOR output has a high power level. With the assistance of EDFA2, the AND output and NOR output have an equal power level with peak power of 1.7mW, which are combined by optical coupler (OC5), thus the mixed signal is XNOR logic, shown in Fig. 19(v). We can observe much noise appears in level "one", which is caused by different modulation intensity in the NOR and AND outputs. As a result, there is a small eye opening ratio with ER of 6dB. When LD2

is turned off, the NOR gate can be simply changed to the NOT gate, as shown in Fig. 19(vi). Good eye pattern can be observed and the ER reaches 11.5dB.

Based on these five logic gates, all-optical digital encoder and comparator could be demonstrated (Wang et al., 2007). As shown in Fig. 20(a) and Fig. 20(c), digital encoder consists of four logic outputs Y0, Y1, Y2, Y3, which are corresponding to four different input conditions. These four different outputs are achieved by four different logic gates: $\overline{A} \cdot \overline{B}$, $\overline{A}B$, $A\overline{B}$ and AB, respectively. For input signal A and B with bits "00", "01", "10" and "11", output bit "1" appears only at port Y0, Y1, Y2 and Y3, respectively.

For digital comparator, three logic outputs are needed to represent three results after comparing the two digital signals. When A is bit "0" and B is bit "1", only the A<B output port is bit "1", and this operation can be represented by $\overline{A}B$ logic. When A and B are both bit "0" or bit "1", only A=B output port is bit "1", and this operation can be represented by $A \odot B$ or XNOR logic. When A is bit "1" and B is bit "0", only the output A>B port is bit "1", this operation can be represented by $A\overline{B}$ logic. From above discussions, we can find that Y1 output in digital encoder is identical with A<B output in comparator and Y2 output is identical with A>B output. In other words, all-optical digital encoder and comparator can be achieved by five different logic functions: $\overline{A} \cdot \overline{B}$, $\overline{A}B$, $A\overline{B}$, AB and $A \odot B$.

Fig. 20(b) shows the principle diagram of proposed scheme for all-optical digital encoder and comparator. Three SOAs are exploited in this scheme. Signal A and B are input signals with wavelength λ_A and λ_B, respectively. SOA1 is used to achieve $\overline{A}B$ logic function at wavelength λ_B based on XGM effect while the optical power of signal A is much larger than signal B. Contrarily, SOA2 is used to achieve $A\overline{B}$ logic function at wavelength λ_A while signal B is much stronger than signal A. Signal A and B are injected into SOA3 together with a continuous wave λ_{cw}. FWM and XGM effects occur simultaneously in SOA3. Based on XGM effect, we can get NOR logic at wavelength λ_{cw}. On the other hand, we can achieve

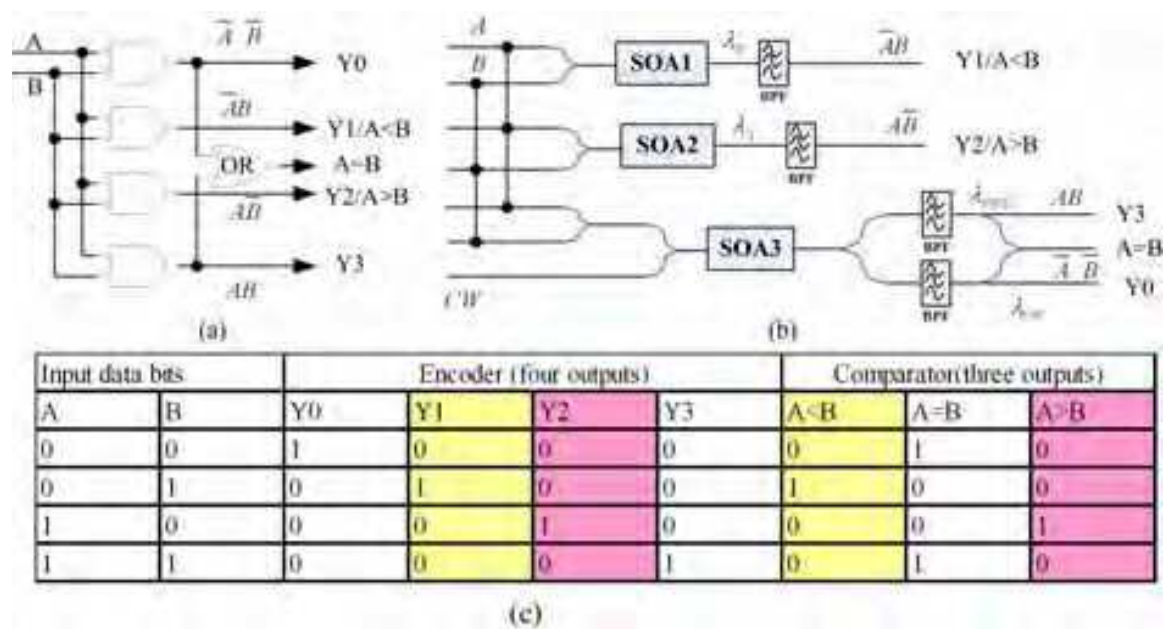| Input data bits		Encoder (four outputs)				Comparator(three outputs)		
A	B	Y0	Y1	Y2	Y3	A<B	A=B	A>B
0	0	1	0	0	0	0	1	0
0	1	0	1	0	0	1	0	0
1	0	0	0	1	0	0	0	1
1	1	0	0	0	1	0	1	0

(c)

Fig. 20. Concept and operation principle of digital encoder and comparator, (a) digital gate-level diagram of encoder/comparator; (b) optical implementation of encoder/comparator; (c) logical truth table for the encoder/comparator

logic AND at the new generated channel based on FWM effect while the optical power of two data signals is nearly equal. Based on the output AND and NOR gates, we can get the XNOR gate by coupling the two outputs together with proper power equalization. Therefore, we can obtain five different logic gates based on XGM or FWM effects in three SOAs, which can be exploited to achieve all-optical digital encoder and comparator simultaneously.

4.3 All-optical minterms generation based on delay interferometer and SOAs

In this sub-section, a general scheme for reconfigurable logic gates for multi-input DPSK signals with integration possibility is proposed (Xu(a) et al., 2008; Xu(b) et al., 2008). Benefiting from the optical logic minterms developed by two kinds of optical devices, i.e., optical delay interferometers and SOAs, target logic functions can be realized by combining specific minterms together. The scheme is reconfigured by changing the phase control of the delay interferometers or the input wavelengths.

In our scheme, DIs and SOAs are used to develop NOT gates and NOR gates, respectively. A DI is a Mach-Zehnder interferometer which has a differential delay τ in one arm and a tunable phase controller Φ_0 in the other, as shown in Fig. 21. τ must equal the bit interval of the given bitrate in order to correctly demodulate DPSK signals while Φ_0 must be tunable to ensure accurate demodulation.
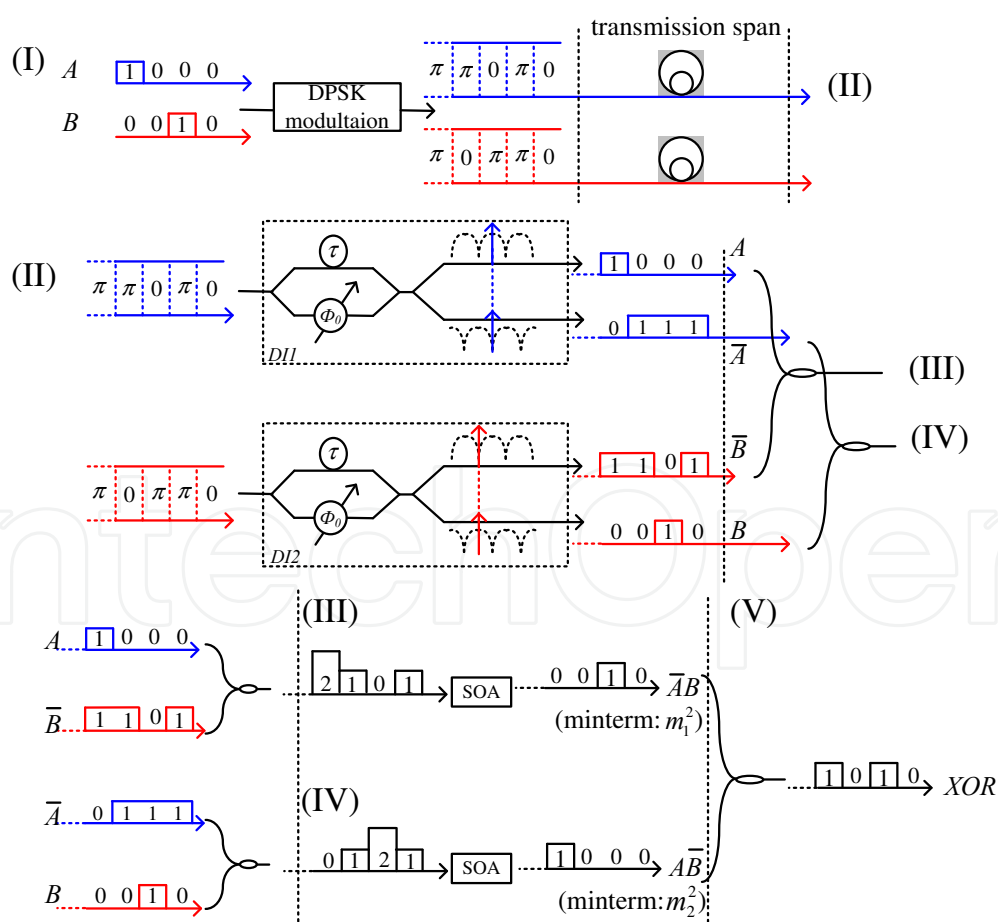
Fig. 21. Logic evolution of two DPSK signals in the generation of optical logic gates from optical minterms based on DIs and SOAs.

In order to explain the operation principle of the scheme, the logic evolutions of DPSK signals through the entire system is briefly described, as shown in Fig. 21. In the first stage (I), two DPSK signals are generated from two absolute binary data *A* and *B* respectively. The coding rule is assumed that '1' is encoded as no phase shift between adjacent bits while '0' is encoded as π shift. After transmission, as shown in the second stage (II), DIs are used to demodulate DPSK signals and recover the original binary data (i.e., *A* or *B* in this case). Note that either the original data or its inversion can be obtained at a certain output of the DI, depending on whether the interference at that port is constructive or destructive. This can be seen from the frequency domain by checking whether the signal wavelength is located on the transmission peak or notch of the spectrum of the concerned output. If the signal wavelength is located on the transmission notch, the spectrum will features as two main peaks with a noticeable notch at its central wavelength. On the other hand, only one main peaks is observed. Based on the illustrated locations of the signal wavelengths on the transmission spectra of the DI (as shown in Fig. 21), *A* (orignial data) shows up in the upper output port of DI1 and $\overline{A}$ (inverted data) in the lower output. Oppositely, *B* is obtained in the lower output of DI2 and $\overline{B}$ in the upper output. In fact, DIs offer a large degree of flexibility of the scheme besides carrying out NOT operation, as will be shown later.

The demodulated signals are combined by optical couplers before launching into the SOAs. It is well known that the cross-gain modulation (XGM) of SOA can be used to carry out NOR operation of nonreturn-to-zero (NRZ) OOK signals. Fig. 22 shows the output probe (λ_2) power of the SOA versus the input pump (λ_1) power. Due to the gain-saturation characteristics of the SOA, the CW probe light will be switched off at the output of the SOA if the input signal power is larger than $P_{in,\,H}$, corresponding to '0' in the output. On the other hand, CW probe light is switched on at the output of the SOA if the input pump power is smaller than $P_{in,\,L}$, corresponding to '1' in the output. For input power between $P_{in,\,L}$ and $P_{in,\,H}$, error logic results will occur. Note that SOA can carry out multi-input NOR operation as well. This is because when one tributary is at ON-state, no matter what states other tributaries are, the total input power during that bit period will exceed $P_{in,\,H}$ and saturate the gain of the SOA to generate '0' at the output. The case that the input DPSK signals are return-to-zero (RZ) format needs to be mentioned. Although the logic integrity is kept, the NOR logic results given by the SOAs will be in dark-RZ pulses due to the characteristics of XGM. To avoid this, other kinds of NOR gates that can process RZ signals can be utilized instead, such as logic gates based on SOAs and optical filtering. In the third stage (III), an SOA can carry out NOR operation of data *A* and $\overline{B}$, creating logic result $\overline{AB}$. Similarly, the other SOA generates $A\overline{B}$ by executing NOR operation of $\overline{A}$ and *B* in stage (IV). In stage (V), final logic $\overline{AB}+A\overline{B}$ is derived by combining the output of stage (III) and (IV) through an optical coupler which functions as an OR gate due to the fact that the probability of concurrence of '1' in different minterms is zero. Therefore, an exclusive-OR (XOR) logic result has been derived. If we change the connection of the optical couplers before stage (III) and (IV) so that the low output port of DI1 is connected to the upper output port of DI2, an XNOR logic ($\overline{\overline{AB}+AB}$) can be obtained. However, the same result can be achieved without changing any physical connections. This is because the DIs can provide a way to exchange the output signals between its two output ports. That is, we can adjust the location of the signal wavelength on the transmission spectra of the DIs to exchange the interference conditions of their two output ports. This can be achieved by tuning Φ_0 of the DIs or

adjusting the wavelengths of the input signals. Note that unlike doing proof-of-concept experiments as what we have done, it is difficult to change the input signals in practical situations. In that case, tuning Φ_0 is the only choice.
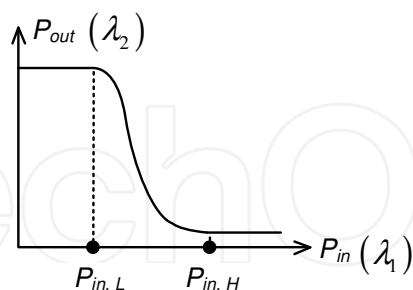

Fig. 22. Output probe power of the SOA versus the input pump power.

Simplified setups are adopted in the experimental trials. That is, a single DI can perform NOT operation for several DPSK signals simultaneously if the input wavelengths can be adjusted. Fig. 23 shows the experimental setup for realizing two-input minterms. Fig. 24 shows the setup for realizing three-input minterms. To facilitate description, important measuring points, i.e., D_{o1}, D_{o2}, S_{i1}, S_{i2}, S_{o1}, S_{o2} and S_{o3}, are marked on Fig. 23 and Fig. 24.
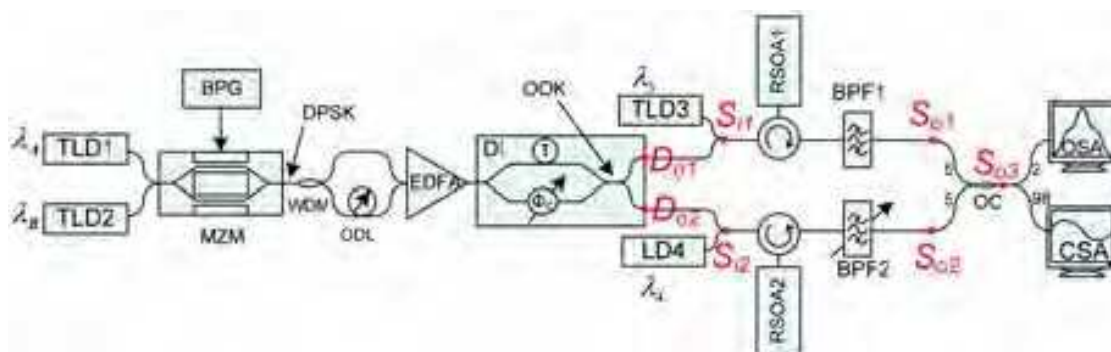
Fig. 23. Experimental setup for two-input NRZ-DPSK logic minterms or logic gates
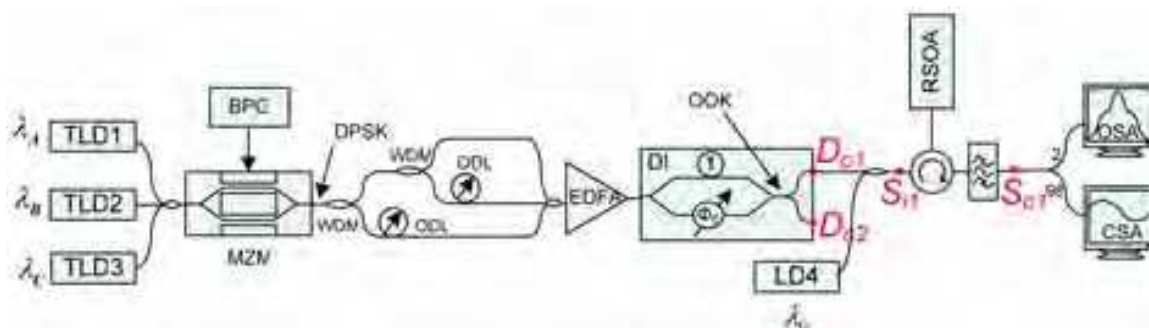
Fig. 24. Experimental setup for three-input NRZ-DPSK logic minterms.

Two-Input Minterms

Due to energy conservation, m_1^2 and m_2^2 appear simultaneously and so does m_0^2 and m_3^2. The signal spectra STO2 shown in Fig. 25(a) are measured at S_{i1} when two-input minterms m_2^2 are derived at S_{o1}. Simultaneously, m_1^2 are obtained at S_{o2} and the spectrum measured at S_{i2} are shown by STO1. In this case, signal at λ_A and λ_B are destructively and constructively demodulated at S_{i1}, respectively. Using the same setup but shifting λ_A downwards by 0.4nm,

both λ_A and λ_B are constructively demodulated at S_{i1}. m_0^2 and m_3^2 are derived at the same time and the spectrum measured at S_{i1} and S_{i2} are shown by STO3 and STO0 in Fig. 25(b).
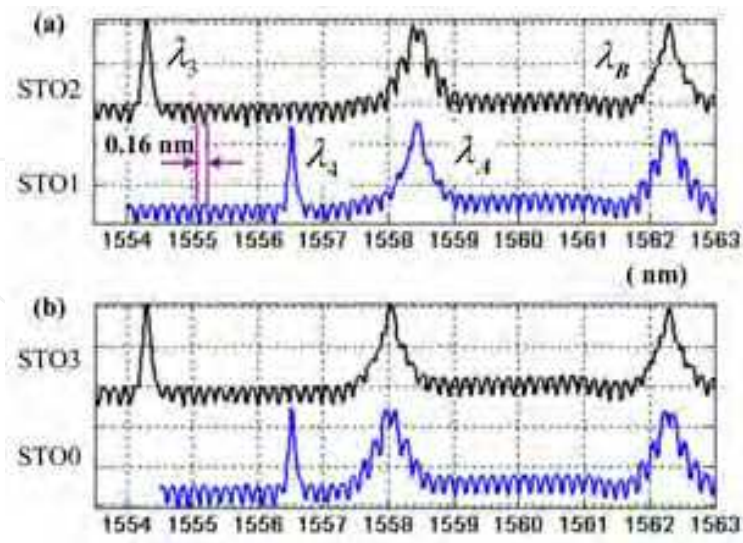

Fig. 25. STO0~STO3: signal spectra measured at S_{i1} or S_{i2} in Fig. 23 when two-input minterms ($m_0^2 \sim m_3^2$) are derived at S_{o1} or S_{o2}.

Fig. 26 shows the measured trace of $m_0^2 \sim m_3^2$ (MTO0 ~MTO3), observed at S_{o1} (MTO1 and MTO2) and S_{o2} (MTO0 and MTO3), respectively. Also shown in Fig. 26 are combined traces CTO0~CTO3 measured at D_{o1} or D_{o2}, corresponding to $\sum(\overline{A},\overline{B})$, $\sum(\overline{A},B)$, $\sum(A,\overline{B})$, and $\sum(A,B)$, respectively. The symbol $\sum$ stands for power superposition. Note that m_0^2 equals NOR logic and m_3^2 equals AND logic. Since m_0^2 and m_3^2 appear at the same time, a simultaneous AND and NOR logic operation can be obtained.
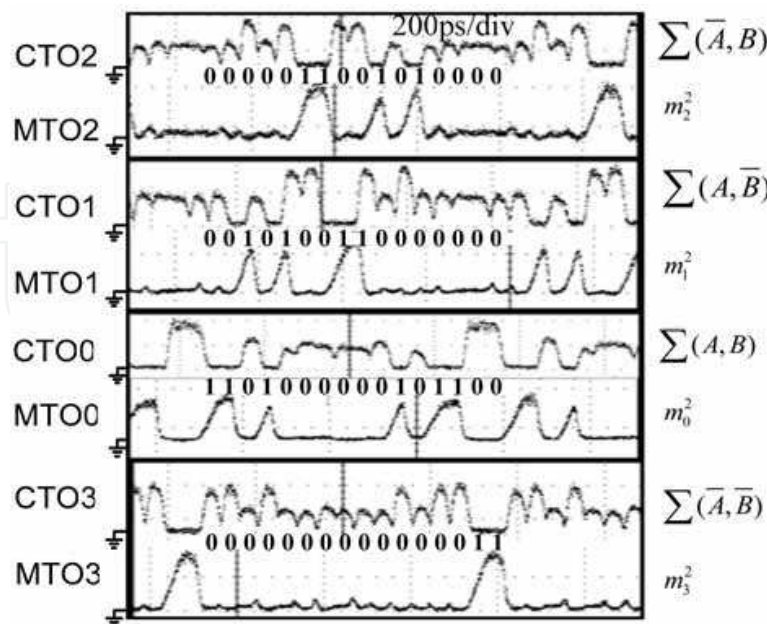
Fig. 26. Measured $m_0^2 \sim m_3^2$ (MTO0~MTO3) as well as the corresponding combined signal measured at D_{o1} or D_{o2} in Fig. 23 (CTO0~CTO3).

Three-Input Minterns

Using the set up shown in Fig.24, eight minterms for three-input DPSK signals are obtained. The temporal waveforms of $m_0^3 \sim m_7^3$ are shown by MTE0~MTE7 in Fig. 26. The temporal waveforms of combined signals measured at D_{o1} when m_7^3 are derived at S_{o1} are shown by CTE7 in Fig. 26 as well. As shown by STE7, $\sum(\overline{A},\overline{B},\overline{C})$ are derived at the input of the RSOA, resulting in m_7^3 after the NOR operation which can be verified by comparing CTE7 and MTE7 in Fig. 26. The full logic integrity of the scheme can be verified by calculating the logic results manually.
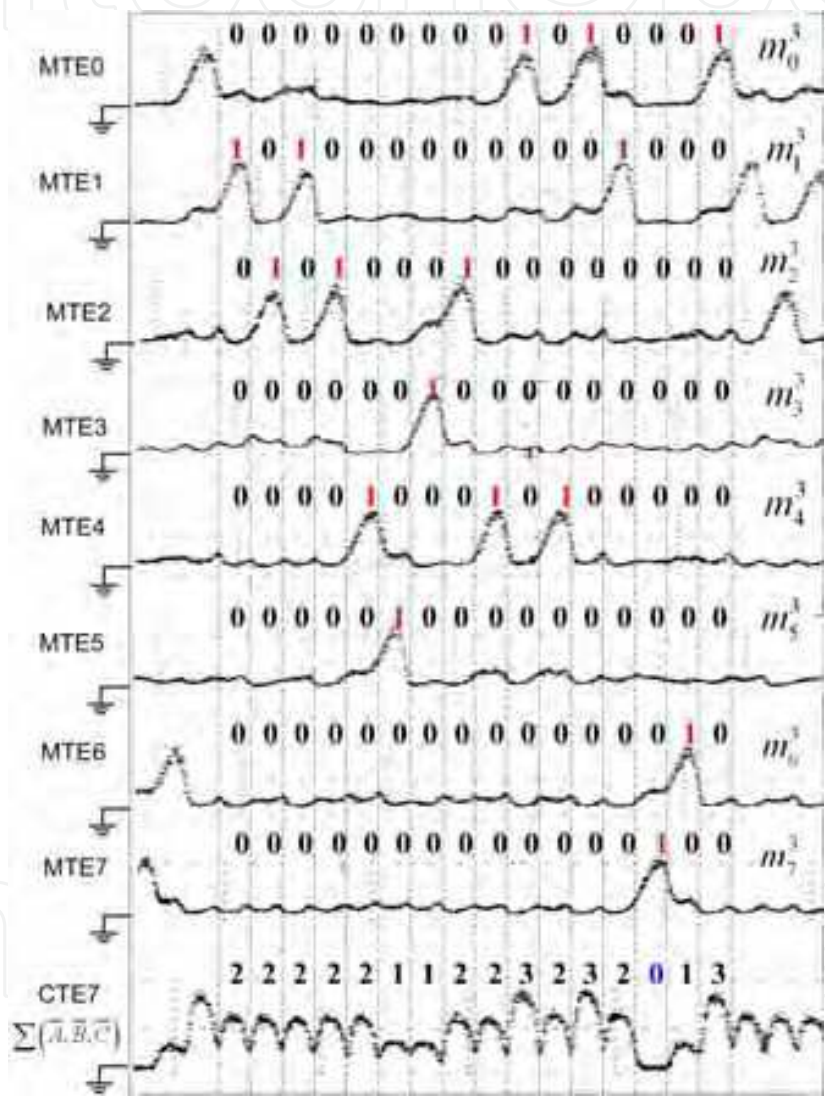
Fig. 26. MTE0~MTE7: measured temporal waveforms of $m_{0\sim7}^3$

In this section, different logic operation functions were demonstrated. Especially, all-optical minterms generation is very important for arbitrary logic functions. On the other hand, these schemes all have potential to be integrated based on SOA and filters. Further investigation should be carried out in order to improve the output performance, increase the operation speed, increase the optical power dynamic range and enhance the stability.

5. Multi-channel regenerative pattern conversion based on SOA and DI

As we know, based on SOA and filter, NRZ-to-RZ conversion for signal channel can be realized while the filter is a little detuning from the central wavelength of the probe NRZ signal (Dong(a) et al., 2007). As shown in Fig.27(a), if multi input channels aim to the transmission spectrum of the DI and are all detuning from the transmission peaks of the comb-like filter (DI) simultaneously, multi-channel NRZ-to-RZ conversion can be realized. As shown in Fig.27(b), the SOA, acting as nonlinear element, causes the broadened spectrum of input NRZ signal due to the XPM effect, and the DI is used to extract the specific spectra from the broadened spectra, for all the 16 channels at the same time. An additional tunable filter with 0.3nm bandwidth is used to filter out one of the converted channels for evaluation (Yu et al., 2008). Simply speaking, the NRZ signals will generate a transient frequency shifts within the control signal duration, and the filter with proper detuning will only transmit frequency shifted components caused by the XPM. For multi-channel operation, in order to minimize the XGM induced inter-channel crosstalk, the SOA should be deeply saturated by the control signal (clock signal).

(a)

(b)
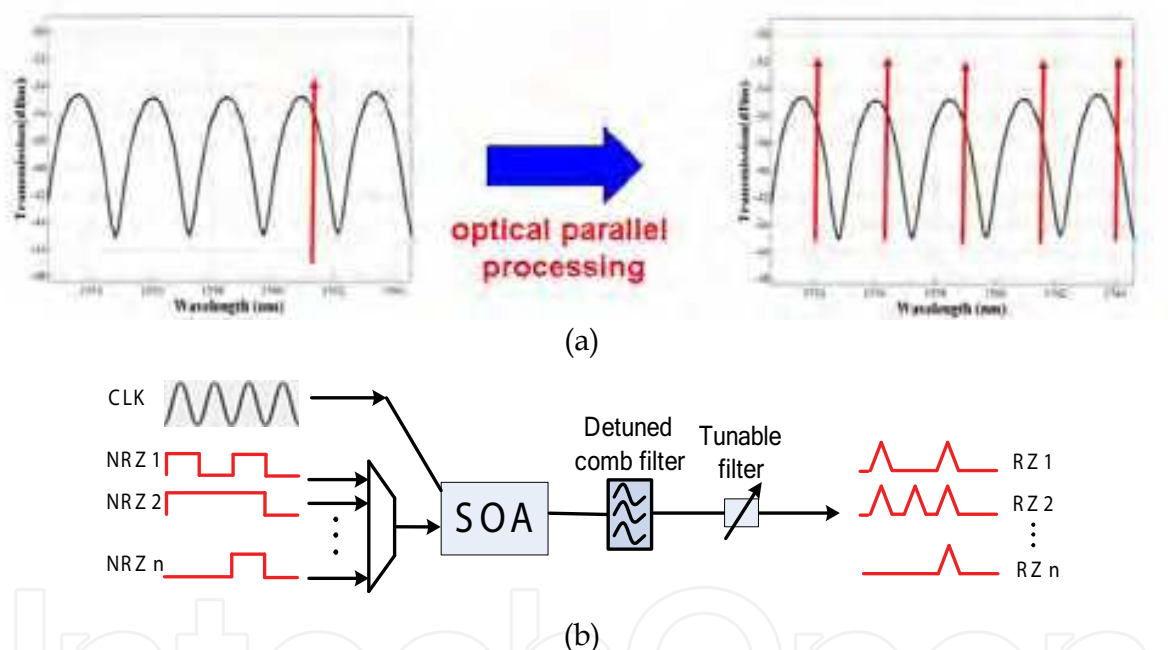
Fig. 27. Operation principle of the multi-channel format conversions: (a) parallel processing principle based on comb filter; (b) schematic diagram for multi-channel pattern conversion scheme.

The experimental setup is shown in Fig. 28 (Yu et al., 2008). 16 channel CW lights from tunable lasers (wavelength from 1547.79 to 1559.79nm with spacing of 0.8nm) are coupled into two MZMs with two AWGs. The odd channels are driven by the RF data (PRBS 2^{31}-1) from Anritsu 10G pattern generator; while the even channels are driven by $\overline{data}$. An optical delay line is added for odd channels to ensure the decorrelation for two data streams. Another CW light (1546.99 nm) is fed into a third MZM, which is driven by the 10GHz RF sine clock signal, to obtain an optical clock signal as the control signal. The delay of the RF clock can be adjusted to synchronize the NRZ signals. Then, the signals are lunched into SOA via a WDM coupler. The average powers of the NRZ signals and the clock signal are

about 3 and 13 dBm before the SOA. The SOA is Kamelian pre-amplifier bias at 160mA. A fiber based DI with free spectral range (FSR) of 0.8nm is used to extract part of each of the broadened DWDM channel spectra. By controlling the operating temperature, its transmission peaks are adjusted to be offset from each carrier wavelength with optimal detuning. Thus, the chirp induced on each channel is passed, while the original spectral components are suppressed to some extent, and hence format conversions from NRZ to RZ can be achieved. A subsequent tunable filter with a 0.3nm 3dB bandwidth is used to filter out one of the converted channels for evaluation.
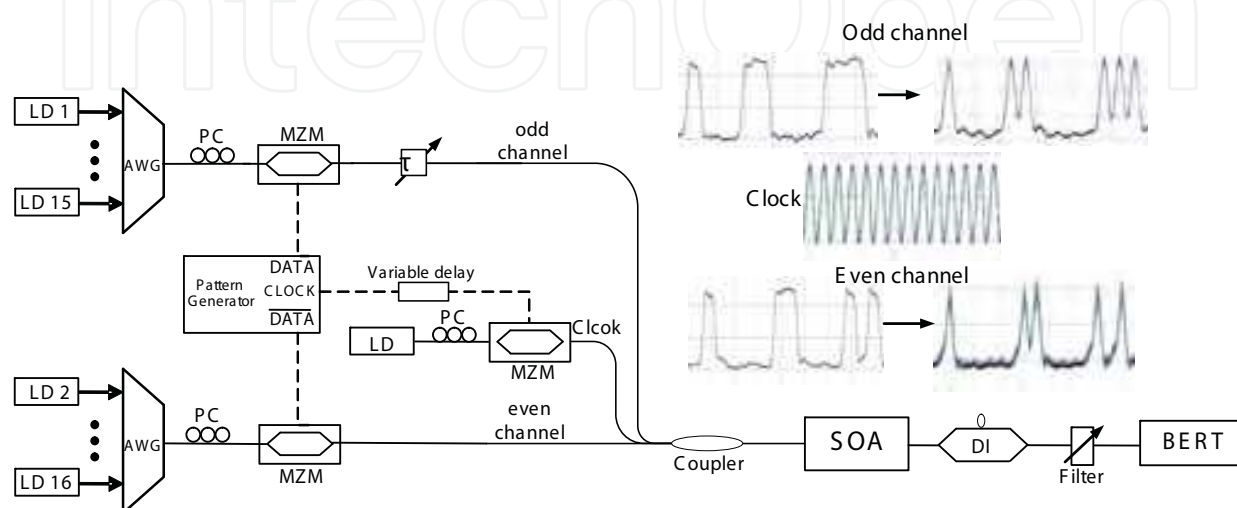
Fig. 28. Experimental setup for 16 channels pattern conversion with SOA and DI

For practical all-optical format conversion, the clock can be recovered from one of the NRZ signals as we have demonstrated in reference (Yu et al., 2006). Since clock extraction is not the purpose of this experiment, for simplicity we obtained the optical clock by modulating a MZM with the RF clock signal directly from the pattern generator.

Since the SOA is deeply saturated by the clock signal, input NRZ signals are only modulated by the XPM, almost without amplitude modulation. Thus, the 16 channels can be with different patterns, which has confirmed by simulation. However, for experimental convenience, only two patterns are used here.

The insets in Fig. 28 show the measured bit stream, both odd and even channels with optimal filter detuning. Results show that the proposed converter works well for different bit pattern simultaneously. The measured spectra before the SOA, after the SOA, after the DI and one of the converted spectra (channel 4) are shown in Fig. 29. It is obvious that all the NRZ spectra are broadened due to the modulation of the clock signal after the SOA, regardless of the spacing between the clock signal and each NRZ signal. The DI filters out the specific part of the spectra periodically.

Taking one of the 16 channels (channel 4) for example; Fig. 30 shows the evolution of the obtained duty cycle as the increase of the DI and the following filter detuning. It can be seen clearly that the pulse width of the converted RZ without detuning is 78 ps, which is wider than the pulse width of the pump clock signal. In other word, the modulation induced by the clock signal is very slight. The pulse width can be significantly compressed to 46 ps with filter detuning of 0.25nm. Although larger detuning can further compress the pulse width, the cross talk from adjacent channel becomes serious.
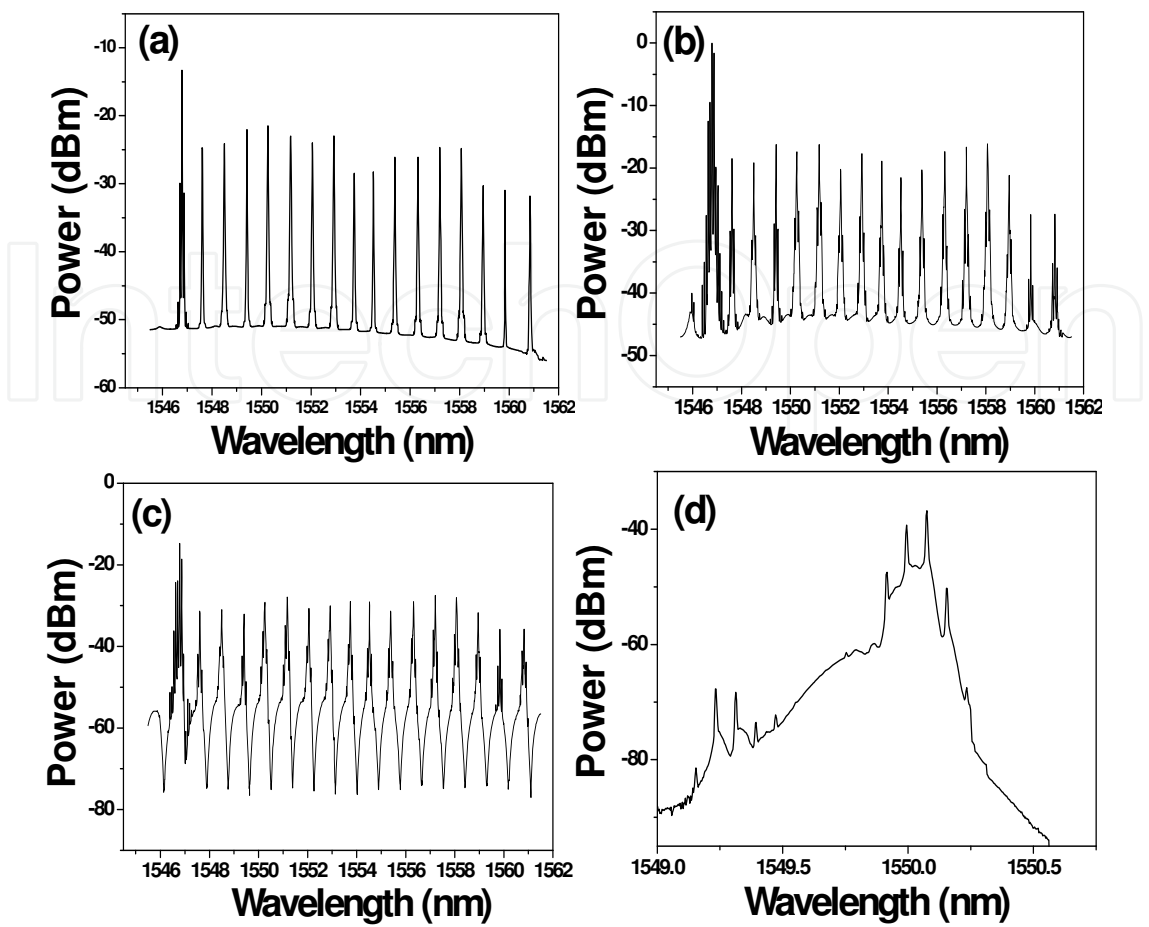
Fig. 29. Spectra of 16 DWDM channels (a) before SOA (b) after SOA (c) after DI and (d) one of the converted channels.

Fig. 31 plots the BER measurements for the format conversions, which are taken for channel 1 (odd channel) and 16 (even channel) and both for three different duty cycles. We can see that negative power penalty can be achieved, for obtained RZ signals with duty cycles of 46, 58 and 69%, respectively. The eye diagram of one channel NRZ signal at back to back is also shown in Fig. 31.
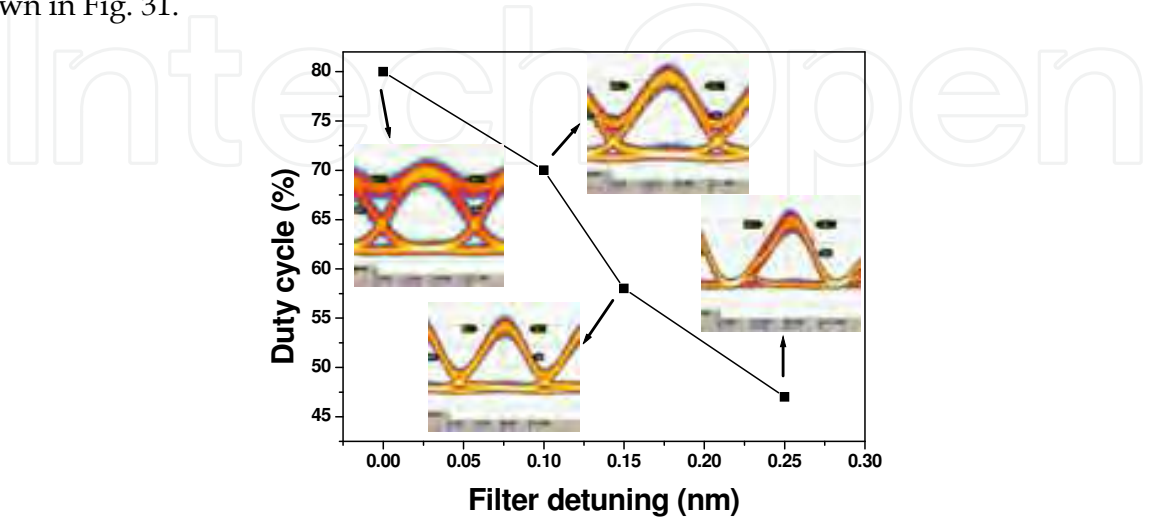

Fig. 30. Duty cycle evolution versus filter detuning
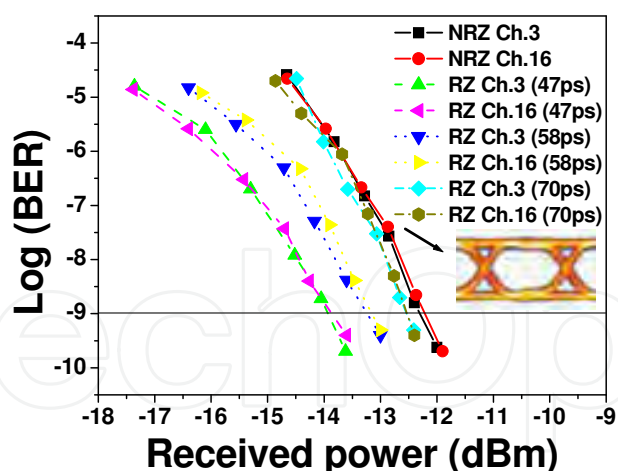
Fig. 31. BER measurements for the conversions
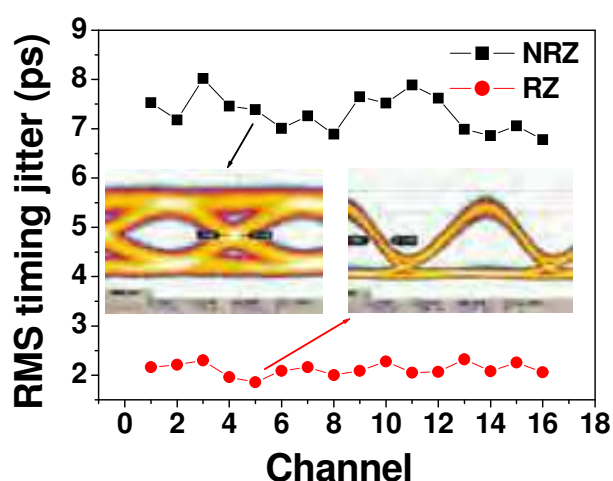
Fig. 32. Measured timing jitter reduction before and after the conversions

Since the clock signal is introduced in the scheme, our proposed converter is regenerative with suppression of timing jitter. To further investigate the retiming performance, the input 16 channel NRZ signals are distorted by attenuating their power and passing them through an EDFA. Fig. 32 presents the RMS timing jitter measurements, more than 3 times jitter reduction can be found for all channels.

6. Conclusions

All-optical signal processing functions are key enabling technologies for signal regeneration and switching in next generation optical networks. SOA has been receiving much attention in all-optical signal processing for its various nonlinear effects and potential to be integrated, and it has been exploited to realize all-kinds of signal processing functions such as all-optical wavelength conversion, all-optical logic operation, all-optical 3R regeneration, all-optical pattern conversion, all-optical sampling, all-optical demultiplexing, etc.

In this chapter, all-optical signal processing based on SOAs and filters was experimental and theoretical investigated. Complicated theoretical model for SOAs is presented, in which besides those conventional effects such as XGM and XPM related to interband recombination process, those ultrafast nonlinear effects such as carrier heating, spectral hole

burning, two-photon absorption are also taken into account. Based on FFT and iFFT tool, filtering process based on different filters can be theoretical analyzed. For those applications with fixed schemes and mechanism, the theoretical model can be used to analyze the output signal performance and optimize the related parameters and operational conditions. Simultaneously, this model can also be used to explore some novel schemes for special signal processing functions. All-optical wavelength conversion for 40Gb/s conventional RZ signals and 80Gb/s RZ signal with ultra-short pulse were experimental realized with SOA and filters. For different filtering process, we can get different wavelength conversion output results, and filtering optimization is very important for improving the output performance. Three schemes for all-optical logic operation were analyzed. Based on cascaded SOAs and related filters, 40Gb/s logic AND gate was demonstrated, in which a slow recovery SOA was exploited in the first stage. Based on various nonlinear effects and different filtering process, configurable five logic gates were achieved. This scheme demonstrated powerful function of SOA with the assistance of filters. Based on demodulation process of DIs and XGM in SOAs, all-optical minterms for two input signals and three input signals were generated. It is possible to demonstrate arbitrary logic functions based on these minterms. Finally, with SOA and comb filter DI, 16 channels pattern conversion at 10Gb/s were effectively demonstrated. Multi-channel signal processing functions are very important for signal regeneration in DWDM optical networks. In further and future investigation, there exist some key points to be noted. First is SOA device optimization, we should find effective and feasible way to accelerate the carrier recovery and enhance the ultrafast nonlinear effects which are the basis for high speed operation, decreasing the needed input power and increasing the flexibility of the scheme. Second is device integration, especially for the scheme based on SOA and DI. InP-based DI is possible to be fabricated, so monolithically integrated SOA and DI structure can be fabricated out, which has potential to be used in multi-channel signal regeneration and all-optical minterms generation. On the other hand, we should pay much attention to all-optical signal processing functions for novel modulation formats, such as DPSK or DQPSK signals. Multi-channel signal processing functions should also receive much more attention because multi-channel optical signal are transmitted in DWDM optical networks.

7. Acknowledgements

8. References

Agrawal, G. & Olsson, N. (1989). Self-Phase Modulation and Spectral Broadening of Optical Pulses in Semiconductor Laser Amplifiers. *IEEE Journal of Quantum Electronics*, vol. 25, No.11, pp 2297-2306, ISSN 0018-9197.

Danielsen, S.; Hansen, P. & Stubkjaer, K. (1998). Wavelength conversion in optical packet switching. *IEEE Journal of Lightwave Technology*, Vol. 16, No.12, pp2095 ~ 2108, ISSN 0733-8724.

Dong(a), J.; Zhang, X.; Xu, J.; Huang, D.; Fu, S. & Shum, P. (2007). 40 Gb/s all-optical NRZ to RZ format conversion using single SOA assisted by optical bandpass filter. *Optics Express,* Vol. 15, No.6, pp2907-2914, ISSN 1094-4087.

Dong(b), J.; Zhang, X.; Wang, Y.; Xu, J. & Huang, D. (2007). 40Gb/s reconfigurable photonic logic gates based on various nonlinearities in single SOA. *Electronics Letters*, Vol.43, No.16, pp884-886, ISSN 0013-5194.

Dong, J.; Zhang, X. ; Fu, S.; Xu, J.; Shum, P. & Huang, D. (2008). Ultrafast all-optical signal processing based on single semiconductor optical amplifier and optical filtering. *IEEE Journal of Selected Topics in Quantum Electronics*, Vol.14, No.3, pp770-778, ISSN 1077-260X.

Durhuus, T.; Mikkelsen, B.; Joergensen, C.; Lykke D. & Stubkjaer, K. (1996). All-optical wavelength conversion by semiconductor optical amplifiers. *IEEE Journal of Lightwave Technology*, Vol.14, No.6, pp942-954, ISSN 0733-8724.

Haché, A. & Bourgeois M. (2000). Ultrafast all-optical switching in a silicon-based photonic crystal. *Applied Physics Letters* Vol.77, No.25, pp4089-4090, ISSN 0003-6951.

Huang, X.; Zhang, Y.; Zhang, Y.; Huang, D. & Zhang, X. (2009). Extinction ratio enhanced 80-Gbit/s wavelength conversion based on optimization of spectrum filtering. *ECOC'2009*, Hongkong, Jul. 2009, FE4.

Kelly, A.; Ellis, A. & Nesset, D. (1998). 100Gbit/s wavelength conversion using FWM in an MQW semiconductor optical amplifier. *Electronics Letters*. Vol. 34, No. 20, pp1955-1956, ISSN 0013-5194.

Langrock, C.; Kumar, S.; McGeehan, J.; Willner, A. & Fejer, M. (2006). All-optical signal processing using $\chi^{(2)}$ nonlinearities in guided-wave devices. *IEEE Journal of Lightwave Technology*, Vol.24, No.7, pp 2579~2592, ISSN 0733-8724.

Liu,Y.; Tangdiongga, E.; Li, Z.; Zhang, S.; DeWaardt, H.; Khoe, G. & Dorren, H. (2006), Error-free all-optical wavelength conversion at 160 Gb/s using a semiconductor optical amplifier and an optical bandpass filter. *IEEE Journal of Lightwave Technology*, Vol. 24, No. 1, pp230-236, ISSN 0733-8724.

Mark, J. & Mørk, J. (1992). Subpicosecond gain dynamics in InGaAsP optical amplifiers: Experiment and theory. *Applied Physics Letters,* Vol. 61, No.19, pp 2281-2283, ISSN 0003-6951.

Mork, J. & Mecozzi, A.(1996). Theory of the ultrafast optical response of active semiconductor waveguide. *J. Opt. Soc. Am. B.*, Vol.13, No.8, pp1803-1816, ISSN 0740-3224.

Mork, J.; Mark, J. & Seltzer, C. P. (1994). Carrier heating in InGaAsP laser amplifiers due to two-photon absorption. *Applied Physics Letters,* Vol. 64, No. 17, pp 2206-2208, ISSN 0003-6951.

Mork, J. & Mark, J. (1995). Time-resolved spectroscopy of semiconductor laser devices: experiments and modeling. *Proceeding of SPIE,* Vol. 2399, pp146-159, Physics and Simulation of Optoelectronic Devices III, Marek Osinski; Weng W. Chow; Eds. Monday 06 February 1995, San Jose, CA, USA.

Olsson, B. & Blumenthal, D. (2001). All-optical demultiplexing using fiber cross-phase modulation (XPM) and optical filtering. *IEEE Photonics Technology Letters*, Vol.13 No.8, pp875~878, ISSN 1041-1135.

Saruwatari M. (2000). All-optical signal processing for terabit/second optical transmission. *IEEE Journal of Selected Topics in Quantum Electronics*, Vol.6, No. 6, pp1363~1374, ISSN 1077-260X.

Stubkjaer K E. (2000). Semiconductor optical amplifier-based all-optical gates for high-speed optical processing. *IEEE Journal of Selected Topics in Quantum Electronics*, Vol.6, No. 6, pp1428~1435, ISSN 1077-260X.

Ta'eed, V.; Shokooh-Saremi, M; Fu, L; Littler, I.; Moss D.; Rochette, M.; Eggleton, B.; Yuan, Y. &Luther-Davies B. (2006). Self-phase modulation-based integrated optical regeneration in chalcogenide waveguides. *IEEE Journal of Selected Topics in Quantum Electronics*, Wol.12, No.3, pp360-370, ISSN 1077-260X.

Wang, Y.; Zhang, X.; Dong, J. & Huang, D.(2007). Simultaneous demonstration on all-optical digital encoder and comparator at 40 Gb/s with semiconductor optical amplifiers. *Optics Express*, Vol.15, No.23, pp15080-15085, ISSN 1094-4087.

Xu, J.; Zhang, X.; Dong, J.; Liu, D. & Huang, D. (2007). Ultrafast all-optical AND gate based on cascaded SOAs with assistance of optical filters. *Electronics Letters*, Vol. 43, No. 10, pp 585-587, ISSN 0013-5194.

Xu(a), J.; Zhang, X.; Dong, J.; Liu, D. & Huang, D. (2008). Simultaneous All-Optical and and nor Gates for NRZ Differential Phase-Shift-Keying Signals. *IEEE Photonics Technology Letters*, Vol.20, No.8, pp596-598, ISSN 1041-1135.

Xu(b), J.; Zhang, X.; Dong, J.; Liu, D. & Huang, D. (2008). All-optical minterm generator for three-input NRZ-DPSK signals based on SOAs and delay interferometers. *OFC/NFOEC*. USA, San Diego, 2008. JWA78.

Yoo S. (1996). Wavelength conversion technologies for WDM network applications. *IEEE Journal of Lightwave Technology,*, Vol.14, No.6, pp955~966, ISSN 0733-8724.

Yu, Y.; Zhang, X. & Huang, D. (2006). All-optical clock recovery from NRZ-DPSK signal. *IEEE Photon. Technol. Lett.*, Vol.18, No.11, pp 2356-2358, ISSN 1041-1135.

Yu, Y.; Zhang, X.; Rosas-Fernández, J.; Huang, D; Penty, R. & White, I. (2008) Single SOA based 16 DWDM channels all-optical NRZ-to-RZ format conversions with different duty cycles. *Optics Express*, Vol.16, No.20, pp16166- 16171, ISSN 1094-4087.

Zhang, X.; Wang, Y.; Sun, J.; Liu, D. & Huang, D. (2004). All-optical AND gate at 10 Gbit/s based on cascaded single-port-coupled SOAs. *Optics Express*, 2004, Vol. 12, No.3, pp 361-366, ISSN 1094-4087.
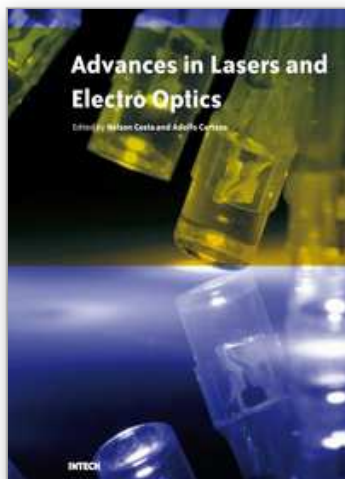
Advances in Lasers and Electro Optics

Edited by Nelson Costa and Adolfo Cartaxo

Lasers and electro-optics is a field of research leading to constant breakthroughs. Indeed, tremendous advances have occurred in optical components and systems since the invention of laser in the late 50s, with applications in almost every imaginable field of science including control, astronomy, medicine, communications, measurements, etc. If we focus on lasers, for example, we find applications in quite different areas. We find lasers, for instance, in industry, emitting power level of several tens of kilowatts for welding and cutting; in medical applications, emitting power levels from few milliwatt to tens of Watt for various types of surgeries; and in optical fibre telecommunication systems, emitting power levels of the order of one milliwatt. This book is divided in four sections. The book presents several physical effects and properties of materials used in lasers and electro-optics in the first chapter and, in the three remaining chapters, applications of lasers and electro-optics in three different areas are presented.

How to reference

In order to correctly reference this scholarly work, feel free to copy and paste the following:

INTECH
open science | open minds